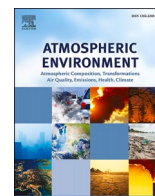




Contents lists available at ScienceDirect

# Atmospheric Environment

journal homepage: <http://www.elsevier.com/locate/atmosenv>

## Size-resolved hygroscopic behaviour and mixing state of submicron aerosols in a megacity of the Sichuan Basin during pollution and fireworks episodes

Liang Yuan<sup>a,b,\*</sup>, Xiaoling Zhang<sup>a,\*\*</sup>, Miao Feng<sup>c</sup>, Xuan Liu<sup>c</sup>, Yuzhang Che<sup>a</sup>, Hanbing Xu<sup>d</sup>, Klaus Schaefer<sup>a</sup>, Shigong Wang<sup>a</sup>, Yunjun Zhou<sup>a</sup>

<sup>a</sup> Plateau Atmosphere and Environment Key Laboratory of Sichuan Province, School of Atmospheric Sciences, Chengdu University of Information Technology, Chengdu, 610225, China

<sup>b</sup> Key Laboratory of Meteorological Disaster (KLME), Ministry of Education & Collaborative Innovation Center on Forecast and Evaluation of Meteorological Disasters (CIC-FEMD), Nanjing University of Information Science and Technology, Nanjing, 210044, China

<sup>c</sup> Chengdu Key Laboratory of Air Pollution Research, Chengdu Academy of Environmental Sciences, Chengdu, 610072, China

<sup>d</sup> Shared Experimental Education Center, Sun Yat-sen University, Guangzhou, 510275, China

### HIGHLIGHTS

- H-TDMA measurements was carried out in a megacity of the Sichuan Basin.
- The hygroscopicity ( $\kappa$ ) was higher than that in Beijing and Guangzhou during winter.
- $\kappa$  during the fireworks episodes were higher than those in the rest of the campaign.

### ARTICLE INFO

**Keywords:**  
Aerosols  
Hygroscopicity  
Mixing state  
H-TDMA  
Chengdu

### ABSTRACT

In-situ measurements were carried out to study the size-resolved hygroscopic behaviour of submicron aerosols during pollution and fireworks episodes in winter from late January to February 2019 in Chengdu, a megacity in Sichuan Basin, using a hygroscopicity tandem differential mobility analyser (H-TDMA). The H-TDMA data were acquired at 90% relative humidity for dry aerosol diameters between 40 and 200 nm. Aerosol particles were usually externally mixed and consisted of nearly hydrophobic mode (NH), less hygroscopic mode (LH) and more hygroscopic mode (MH) in the urban area. The average ensemble mean hygroscopicity parameter values ( $\kappa_{\text{Mean}}$ ) over the entire sampling period were 0.16, 0.19, 0.21, 0.23 and 0.26 for aerosols with diameters of 40, 80, 110, 150 and 200 nm, respectively. These averages were lower than those in Shanghai and Nanjing.  $\kappa_{\text{Mean}}$  for aerosols larger than 110 nm, however, were higher than those in Beijing and Guangzhou during winter. Distinct diurnal patterns for all measured sizes were observed for aerosol hygroscopicity and mixing state because of the photochemical reactions and the activities of the planetary boundary layer (PBL). The number fractions of the NH ( $N_{\text{F,NH}}$ ) was low, but  $\kappa_{\text{Mean}}$  was high, and more aerosols were internally mixed during daytime. The number fraction of LH ( $N_{\text{F,LH}}$ ) for the 40-nm diameter aerosols in clean periods (CPs) was larger than that in the pollution episodes (PEs) because of the increasing amount of SOA formation. More aerosols of diameters larger than 80 nm were internally mixed during CPs and pollution accumulation period, resulting in higher  $\kappa_{\text{Mean}}$  values. More strong hygroscopic components of fireworks were found in the larger aerosols during the fireworks episode (FE). The average  $\kappa_{\text{Mean}}$  values of 0.19, 0.19, 0.21, 0.23 and 0.27 for the 40, 80, 110, 150 and 200-nm diameter aerosols, respectively, during the FE were higher than those during the pre- and post-FE periods. The findings of this study contribute to the preliminary understanding of the hygroscopic behaviour of urban aerosol particles in the Sichuan Basin, which are essential for understanding the formation and evolution of severe haze events in the Sichuan Basin.

\* Corresponding author. Plateau Atmosphere and Environment Key Laboratory of Sichuan Province, School of Atmospheric Sciences, Chengdu University of Information Technology, No.24 Block 1, Xuefu Road, Chengdu, 610225, China.

\*\* Corresponding author. Plateau Atmosphere and Environment Key Laboratory of Sichuan Province, School of Atmospheric Sciences, Chengdu University of Information Technology, No.24 Block 1, Xuefu Road, Chengdu, 610225, China.

E-mail addresses: [yuanl\\_nuist@outlook.com](mailto:yuanl_nuist@outlook.com) (L. Yuan), [xlzhang@ium.cn](mailto:xlzhang@ium.cn) (X. Zhang).

<https://doi.org/10.1016/j.atmosenv.2020.117393>

Received 30 November 2019; Received in revised form 22 February 2020; Accepted 8 March 2020

Available online 17 March 2020

1352-2310/© 2020 Elsevier Ltd. All rights reserved.

## 1. Introduction

Aerosol hygroscopicity describes the interaction of aerosols and water vapour under sub-saturated and super-saturated conditions. Thus, this property plays an important role in the study of aerosol radiative forcing and atmospheric processes, which influence aerosol life cycle, activation ability and climate effects (Swietlicki et al., 2008; Tao et al., 2012; Bian et al., 2014). The hygroscopic growth of aerosols at an elevated relative humidity (*RH*) alters their particle size, refractive indices and phase function. The change in diameter experienced by the aerosol due to water uptake can modify the scattering and absorption properties, which significantly influence aerosol direct radiative forcing and severely threaten atmospheric visibility (Liu et al., 2013a, 2013b; Tie et al., 2017). Aerosol hygroscopicity also determines whether aerosols can be activated as cloud condensation nuclei (CCN) under given super-saturated water vapour conditions (Petters and Kreidenweis, 2007), which considerably affect aerosol indirect radiative forcing. Furthermore, hygroscopic aerosols can provide a liquid water medium for chemical processes (ageing process), which has reverse influence on the aerosol chemical composition (Herrmann et al., 2015; Tan et al., 2016; Li et al., 2017).

To describe the hygroscopic growth of aerosol particles, the hygroscopicity parameter,  $\kappa$ , representing the aerosol water uptake capacity, is widely applied and successfully used in numerous studies for both single-component and multi-component particles (Petters and Kreidenweis, 2007). This parameter was proposed in  $\kappa$ -Köhler theory by Petters and Kreidenweis (2007); it is proved to be a considerably effective parameter for investigating aerosol hygroscopicity and its impact on aerosol optical properties, aerosol liquid water contents and CCN activation (Zieger et al., 2013; Bian et al., 2014; Chen et al., 2014; Tao et al., 2014; Kuang et al., 2015; Brock et al., 2016). The parameter makes the comparison of aerosol hygroscopicity at different sites and different time periods around the world more convenient. Moreover,  $\kappa$  also facilitates the inter-comparison of aerosol hygroscopicities derived by various techniques and measurements made under different *RH* levels.

Two of the most popular techniques to measure the hygroscopic behaviour of atmospheric aerosols are the humidified nephelometer system (Carrico et al., 2000; Kuang et al., 2017) and the hygroscopicity tandem differential mobility analyser (H-TDMA) (Liu et al., 1978). The humidified nephelometer system measures the aerosol light scattering enhancement, which can be used to calculate the optically weighted  $\kappa$  which is the overall hygroscopicity of ambient aerosol particles, if the particle number size distribution (PNSD) of dry aerosols is measured simultaneously (Chen et al., 2014; Kuang et al., 2017). The H-TDMA measures the hygroscopic growth as a function of aerosol diameter and *RH*. This system can therefore provide information that related to the aerosol hygroscopicity at different diameters. Thereafter,  $\kappa$  and the mixing state of aerosol with various diameters can be directly calculated and derived from the H-TDMA measurements.

Previous works that employed H-TDMA were summarised by Swietlicki et al. (2008) and Alonso-Blanco et al. (2019). The H-TDMA measurements were performed at various environments in Europe (Massling et al., 2005; Štefancová et al., 2010; Adam et al., 2012; Kamilli et al., 2014; Enroth et al., 2018), North America (Cocker et al., 2001; Levy et al., 2014) and Asia (Chen et al., 2003; Kim et al., 2017; Müller et al., 2017). In China, a number of studies in this regard were conducted and mainly implemented in developed megacities, such as Beijing (Wu et al., 2016; Wang et al., 2017; Wang et al., 2018c), Tianjin (Liu et al., 2011), Shanghai (Ye et al., 2011, 2013), Nanjing (Wu et al., 2014; Li et al., 2015), Guangzhou (Tan et al., 2013b; Jiang et al., 2016) and Hongkong (Yeung et al., 2014) in recent years. These investigations showed that ambient aerosol particles are generally divided into two or three groups: nearly hydrophobic mode (NH), less hygroscopic mode (LH) and more hygroscopic mode (MH). The nearly hydrophobic aerosols are dominated by carbonaceous aerosols generated from the

combustion of fossil fuels and biomass. The less hydrophilic aerosols are usually moderately modified carbonaceous aerosols resulting from condensation or coagulation processes or newly formed organic aerosols generated during photochemical processes. The more hygroscopic mode consists of secondary inorganic salts, such as sulphate, nitrate and ammonium (Liu et al., 2011; Tan et al., 2013b; Wang et al., 2018c). The fraction contribution of each mode varies depending on dry particle size, time period and season (Massling et al., 2009; Wu et al., 2016). Different emission patterns contribute to different hygroscopicities and mixing states of aerosols. The ageing process is also an important factor that influences the mixing state of aerosol particles, thus impacting aerosol hygroscopicity (Boreddy et al., 2015; Wu et al., 2016; Wang et al., 2018d). For example, freshly emitted soot particles are hydrophobic and could possibly become strongly hygroscopic and efficient CCN through the ageing process in highly polluted areas over a short time period (Khalizov et al., 2009). Tan et al., (2013b) and Wang et al. (2017) reported that aerosols are probably internally mixed with a homogeneous chemical composition during clean periods.

The Sichuan Basin is located to the east of the Tibetan Plateau. It is encircled by high mountains and plateaus and characterised by persistently high *RH* and extremely low wind speeds all year round (Liao et al., 2018; Ning et al., 2018). The microphysical properties of aerosols in the deep areas of Sichuan Basin are assumed to considerably differ from those in the regions mentioned above because of the basin's distinct topography and meteorological conditions. Chengdu is one of the largest cities in the Sichuan Basin, with a population exceeding 16 million and vehicles numbering more than 5 million in 2018 (<http://tjj.sc.gov.cn>). The annual average *RH* of 82% in Chengdu is higher than those of the cities at the same latitude, such as Wuhan (80%), Nanjing (73%) and Shanghai (75%) (2018, <http://www.stats.gov.cn/>). Chengdu is an excellent site to investigate the relationship between ambient aerosols and water vapour. Considerable amounts of aerosols absorb water vapour under high *RH* conditions, which may have a significant contribution to the heavy haze formation in Chengdu and Sichuan Basin. The number of studies that discuss the hygroscopicity in this region, however, are limited, and direct measurements of size-resolved hygroscopicity barely exist.

This study therefore aims to (1) obtain the size-resolved hygroscopicity of submicron aerosol in Chengdu; (2) investigate the key factors that influence the variation of hygroscopicity parameter and aerosol mixing state; (3) elucidate the impacts of fireworks on aerosol hygroscopicity.

## 2. Measurements and methodology

### 2.1. Site description

The campaign was implemented from 23 January to 25 February 2019 at the meteorological station (30.58°N, 103.98°E) inside the campus of Chengdu University of Information and Technology (CUIT) located in the Shuangliu district, which is southwest of the main urban area of Chengdu, China. The elevation of the observation site is approximately 500 m. Fig. 1 shows the map of the site. It is surrounded by residential neighbourhoods with no nearby sources of significant industrial pollution.

### 2.2. Instrumentation

A custom-built H-TDMA designed by Tan et al., (2013a) was employed. This instrument can be alternately operated as a Scanning Mobility Particle Sizer (SMPS) or a H-TDMA. The PNSDs was observed by the SMPS and the hygroscopic growth factor (*GF*) was determined by the H-TDMA. It was placed in a temperature-controlled container (25 °C). The aerosol inlet was equipped with a PM<sub>2.5</sub> impactor that extended out of the container from the roof and set approximately 3 m above ground. This instrument was applied in the previous studies of Jiang

et al. (2016), Wang et al. (2017), Wang et al. (2018c) and Wang et al. (2018d). The detailed description of this instrument was reported by Tan et al. (2013a).

Briefly, this instrument mainly consists of two differential mobility analysers (DMA) (Model 3081A, TSI Inc., USA), a humidification system and a condensation particle counter (CPC) (Model 3787, TSI Inc., USA). The aerosols are first sampled with a flow of 0.6 L/min by making them pass through a Nafion dryer (Model MD-700-24S-3, Perma Pure Inc., USA) to maintain the *RH* level below 10%. The aerosols thereafter are charged after flowing through an advanced aerosol X-ray neutraliser (Model 3088, TSI Inc., USA). When the system works as the SMPS, the charged aerosols pass through the first DMA (DMA1) with continuously changed voltage and then directly flows into the CPC. Finally, the PNSDs under dry condition is obtained. When the system works as the H-TDMA, the charged aerosols pass through the first DMA (DMA1) with set voltage and then aerosols with a specific dry diameter is selected. The selected quasi-monodisperse dry aerosols are subsequently introduced into a Nafion humidifier (Model PD-07018T-24MSS, Perma Pure Inc., USA) where they are exposed to water vapour and humidified to an *RH* of 90% with a  $\pm 0.3\%$  variation; the residence time is 10 s. Finally, the PNSDs of humidified particles resulting from the humidifier are measured by the second DMA (DMA2) coupled with the CPC. The growth factor (*GF*) of the quasi-monodisperse aerosols selected by DMA1 ( $GF(D_p(\text{Dry}))$ ) can be then calculated by

$$GF(D_p(\text{Dry})) = \left( \frac{D_p(\text{RH})}{D_p(\text{Dry})} \right) \quad (1)$$

where  $D_p(\text{RH})$  represents the particle diameter measured at an *RH* of 90%, and  $D_p(\text{Dry})$  denotes the selected diameter under dry conditions ( $\text{RH} \leq 10\%$ ). The measured distribution function (MDF) of *GF* (*GF*-MDF) can be calculated from the particle number concentration obtained by the CPC downstream from DMA1 and DMA2. The switch of the SMPS and the H-TDMA and the data acquisition are automatically controlled by a custom LabVIEW software (Tan et al., 2013a).

In this campaign, the SMPS measured the PNSDs of dry aerosol particles between 10 and 400 nm in 75 size bins. The H-TDMA measured the *GF* at an *RH* of 90% for aerosols with five selected dry diameters, including 40, 80, 110, 150 and 200 nm. One data acquisition cycle of H-TDMA included one SMPS scanning and one *GF*s measurement for the five selected diameters. This lasted for approximately 60 min (5, 40 and 15 min for obtaining dry PNSD, *RH* equilibrium in DMA2 and five *GF*s, respectively). The H-TDMA calibration was conducted every two weeks using standard polystyrene latex spheres and ammonium sulphate.

The mass concentration of black carbon (BC) in  $\text{PM}_{2.5}$  was measured by an Aethalometer (Model AE33, Magee Scientific Co. Ltd., USA). The hourly organic carbon (OC) content in  $\text{PM}_{2.5}$  was measured by a Semi-

continuous Thermal-Optical Transmittance carbon analyser (Model RT-4, Sunset Laboratory Inc., Tigard, Oregon, USA). The water-soluble inorganic ions in  $\text{PM}_{2.5}$  with a temporal resolution of 1 h were obtained by an In-situ Gas and Aerosol Compositions monitor (Model S-611EG, Fortelice International Co., Ltd., Taiwan). The validation of these three instruments could be found elsewhere (Bauer et al., 2009; Jing et al., 2019; Liu et al., 2019).

The meteorological data at Shuangliu weather station were derived from the China Meteorological Data Service Center (<http://data.cma.cn/>). The data included temperature (*T*), *RH*, precipitation (*P*), wind direction (*WD*) and wind speed (*WS*). The planetary boundary layer (PBL) height was obtained from the ERA5 reanalysis data (<https://cds.climate.copernicus.eu/>). The atmospheric pollutant data of  $\text{PM}_{10}$ ,  $\text{PM}_{2.5}$ , CO, SO<sub>2</sub>, NO<sub>2</sub> and O<sub>3</sub> were derived from the environmental monitoring station of Chengdu (<http://sthj.chengdu.gov.cn/>). The temporal resolution of these data was 1 h.

### 2.3. Methodology

The TDMA<sub>fit</sub> algorithm (Stolzenburg and McMurry, 2008) was employed to convert the *GF*-MDF to the actual probability distribution function of *GF* (*GF*-PDF) (Gysel et al., 2009) in the campaign. The same algorithm was widely applied in Beijing (Wang et al., 2017; Wang et al., 2018a), Nanjing (Wu et al., 2014) and Guangzhou (Tan et al., 2013b; Jiang et al., 2016). It corrects the discrepancies attributed by the diffusing transfer function in the DMA and describes the *GF*-PDF as a sum of one or more lognormal distribution functions. The *GF*-PDFs are thereafter normalised as  $\int c(g)dg = 1$  for each measured dry diameter, where *g* represents *GF* and *c*(*g*) represents the normalised *GF*-PDF.

Three modes (NH, LH and MH) of aerosol particles were frequently and repeatedly found in *GF*-PDF during the campaign because of the complex chemical composition of ambient aerosols. Each mode was categorised based on the *GF* value as shown in Fig. S1 (the supplemental file).

NH mode:  $GF \leq 1.10$

LH mode:  $1.10 < GF \leq 1.33$

MH mode:  $GF > 1.33$

The ensemble mean growth factor ( $g_{\text{Mean}}$ ) at each measured size is defined as the volume equivalent mean growth factor of the *GF*-PDF over the entire *GF* range.

$$g_{\text{Mean}} = \left( \int g^3 c(g) dg \right)^{\frac{1}{3}} \quad (2)$$

The number fraction (*NF*) and mean *GF* for each hygroscopic mode is

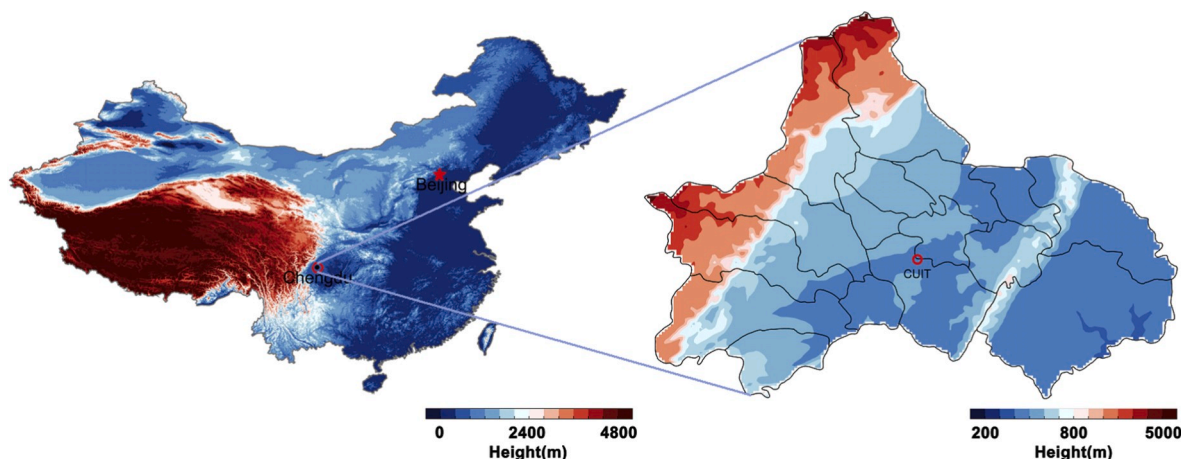


Fig. 1. Location of the observation site.

calculated as

$$NF_{\text{NH; LH; MH}} = \int_{g_1}^{g_2} c(g)dg \quad (3)$$

and

$$g_{\text{NH; LH; MH}} = \left( \frac{\int_{g_1}^{g_2} g^3 c(g)dg}{\int_{g_1}^{g_2} c(g)dg} \right)^{\frac{1}{3}} \quad (4)$$

where  $g_1$  and  $g_2$  are the boundaries of each mode.

The mixing state of aerosol particles in terms of hygroscopic growth can be derived from the *GF*-PDF. A wide spread of *GF*-PDF generally indicates an external mixture of aerosols. The standard deviation of *GF*-PDF ( $\sigma_{GF\text{-PDF}}$ ) (Eq. (5)) is therefore generally used as a reference to discuss the mixing state of the submicron aerosols (Sjogren et al., 2008; Liu et al., 2011; Jiang et al., 2016).

$$\sigma_{GF\text{-PDF}} = \left( \int (g - g_{\text{Mean}})^2 c(g)dg \right)^{\frac{1}{2}} \quad (5)$$

In order to facilitate the comparison of measurements at different *RH* levels, the hygroscopicity parameter,  $\kappa$ , is calculated based on  $\kappa$ -Köhler theory (Petters and Kreidenweis, 2007):

$$\kappa = (GF^3 - 1) \cdot \left[ \frac{1}{RH} \cdot \exp\left(\frac{4\sigma_{s/a}M_w}{RT\rho_w D_p(\text{Dry})GF}\right) - 1 \right] \quad (6)$$

where  $\sigma_{s/a}$  (0.072 J/m<sup>2</sup>) is the surface tension of the solution/air interface;  $M_w$  (18.015 g/mol) is the molecular weight of water;  $\rho_w$  (1.0 g/cm<sup>3</sup>) is the density of water;  $R$  (8.3145 J/K·mol) is the universal gas constant;  $T$  (298.15 K) is the temperature. For each *GF*-PDF, the probability distribution function of  $\kappa$  ( $\kappa$ -PDF) can be converted using Eq. (6). The ensemble mean hygroscopicity parameter ( $\kappa_{\text{Mean}}$ ) and  $\kappa$  for the three modes ( $\kappa_{\text{NH}}$ ,  $\kappa_{\text{LH}}$  and  $\kappa_{\text{MH}}$ ) can be also calculated from  $g_{\text{Mean}}$ ,  $g_{\text{NH}}$ ,  $g_{\text{LH}}$  and  $g_{\text{MH}}$ .

### 3. Results and discussion

#### 3.1. Meteorological conditions during the sampling period

During the campaign, the weather conditions were dominated by

cloudy days, and only a few days were clear. Fig. 2 shows the meteorological parameters, including *WD*, *WS*, *T*, *RH*, *P*, visibility and atmospheric pressure during the observation period (Local Standard Time, LST). Parameters *T* and *RH* showed evident diurnal cycles with average values of  $8.4 \pm 3.0$  °C and  $76.6\% \pm 16.4\%$ , respectively. The winds that prevailed were northerly, with an average *WS* of  $1.0 \pm 0.7$  m/s, and the atmospheric pressure periodically fluctuated. Several light rains occurred on the nights of 30 January and 14, 23 and 24 February, as shown in Fig. 2. Continuous precipitation occurred from the early morning of 17 February to the following morning, which was attributed to the southward motion of cold air. The visibility widely varied between 0.1 and 23.3 km with an average of 5.1 km.

#### 3.2. Overview of measurements

##### 3.2.1. Time series of pollutants and differentiation into typical pollution events

Fig. 3 shows the time series of the mass concentration of four trace gases (SO<sub>2</sub>, NO<sub>2</sub>, O<sub>3</sub> and CO), PM<sub>2.5</sub> and PM<sub>10</sub> over the entire observation period. The BC mass concentrations and the PNSDs with diameters between 10 and 400 nm are also presented in Fig. 3. Large temporal variations and different trends were found for each trace gas; PM<sub>2.5</sub>, PM<sub>10</sub> and BC followed the same trends with campaign averages of 78.9106.1 and 5.0 μg m<sup>-3</sup>, respectively. Generally, PM<sub>2.5</sub> and PM<sub>10</sub> agreed well with SO<sub>2</sub> and the correlation coefficients between PM and SO<sub>2</sub> were 0.74–0.78 during the whole period. Although the correlation coefficients between PM and CO were low (0.34 and 0.36), they have the same variation trends during some periods in the campaign. This indicated the same type of sources of PM, SO<sub>2</sub> and CO in these periods. Additionally, the obvious diurnal pattern could be found for the variation of O<sub>3</sub> on sunny days, indicating the strong photochemical reactions. According to the time series of PM and the PNSDs, the high values of PM were often corresponding to the high number concentration of aerosols larger than 100 nm. This revealed the large contribution of aerosols larger than 100 nm to PM. The PNSDs also showed several ageing processes with the median of particle dimeters increasing gradually with time. Three pollution events (PEs) and one fireworks episode (FE), in which increase PM<sub>2.5</sub> could be observed, were highlighted as case studies to further analyse the difference among aerosol hygroscopicities during different time periods. There were no obvious peak values of CO

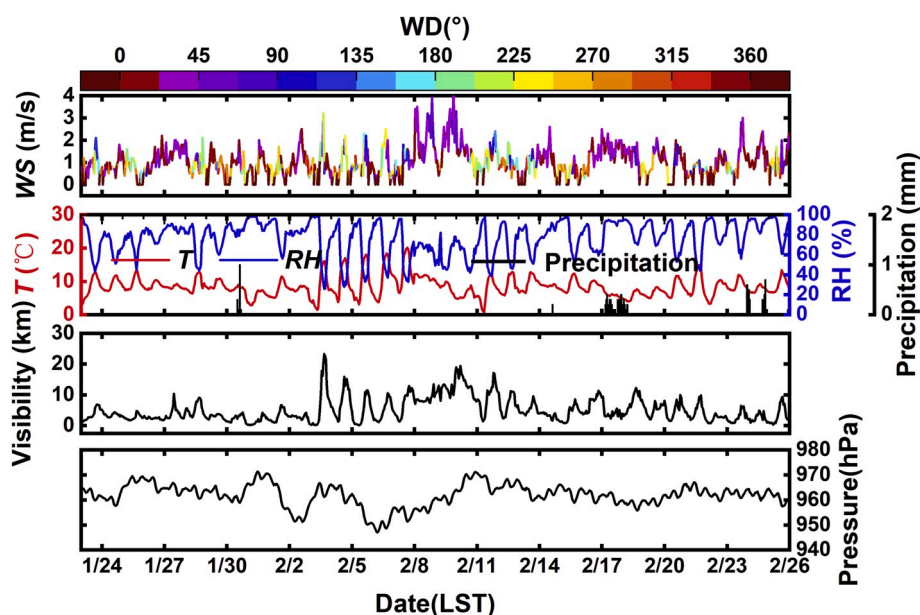


Fig. 2. Time series of (a) hourly wind direction (*WD*) and wind speed (*WS*), (b) temperature (*T*), relative humidity (*RH*) and precipitation (*P*), (c) visibility and (d) atmospheric pressure during the observation period.

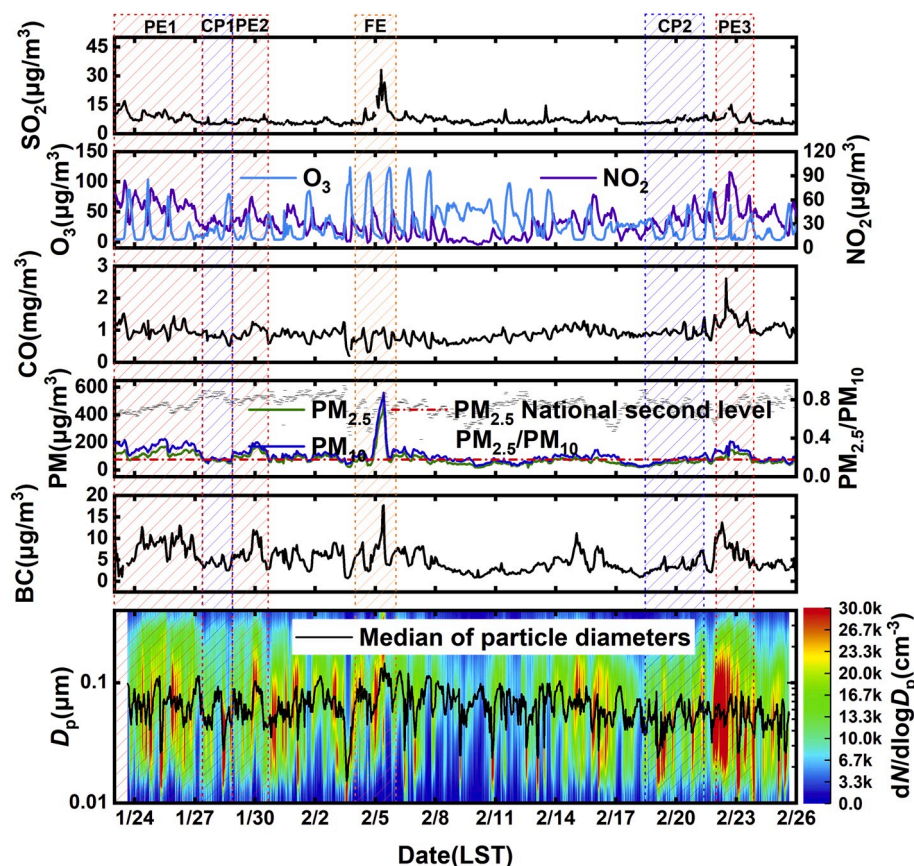


Fig. 3. Time series of (a)  $\text{SO}_2$ , (b)  $\text{NO}_2$  and  $\text{O}_3$ , (c)  $\text{CO}$ , (d)  $\text{PM}_{2.5}$  and  $\text{PM}_{10}$ , (e) mass concentration of  $\text{BC}$  and (f) aerosol number size distribution (PNSD) with diameters between 10 and 400 nm over the entire observation period.

during FE compared to the rest of the period and the  $\text{CO}$  concentration was just a little higher than the campaign average at the time when  $\text{PM}_{2.5}$ ,  $\text{PM}_{10}$  and  $\text{SO}_2$  reached the top during FE. The same variation trend of  $\text{CO}$  as  $\text{PM}_{2.5}$  and  $\text{PM}_{10}$ , however, occurred during FE, indicating the influence of fireworks on these pollutants. On 17 February, the  $\text{PM}$  concentrations evidently decreased because of wet deposition, which can also be observed from the PNSDs shown in Fig. 3. The effects of these pollutants on aerosol hygroscopicity will be further discussed in detail.

### 3.2.2. Characteristics of particle hygroscopic properties

Fig. 4 shows the time series of  $\kappa$ -PDF for aerosols with diameters of 40, 80, 110, 150 and 200 nm during the campaign. In Fig. 4, the pink, black and light grey lines represent  $N_{\text{FNH}}$ ,  $\kappa_{\text{Mean}}$  and  $\sigma_{\text{GF-PDF}}$  time series, respectively. The peak value of  $\kappa$ -PDF existed in the NH mode for the 40-nm aerosol particles and generally shifted to the MH mode with increasing particle size. This indicated that the MH mode increasingly becomes more prominent with increasing size. For all particle sizes measured,  $\kappa_{\text{Mean}}$  practically followed the same trend with evident temporal variability. A reverse trend was exhibited by  $N_{\text{FNH}}$  in relation to the  $\kappa_{\text{Mean}}$ . This was mainly attributed to the fact that  $\kappa_{\text{Mean}}$  was considerably determined by  $N_{\text{FMH}}$ , which was contrary to  $N_{\text{FNH}}$ .

The size-dependent  $\kappa$  and  $N_{\text{F}}$  values for NH, LH and MH modes ( $\kappa_{\text{NH}}$ ,  $\kappa_{\text{LH}}$ ,  $\kappa_{\text{MH}}$  and  $N_{\text{FNH}}$ ,  $N_{\text{FLH}}$  and  $N_{\text{FMH}}$ , respectively) for the whole campaign were parameterised as a function of dry diameter,  $D_{\text{p}}(\text{Dry})$ , using Eq. (7) (Rissler et al., 2006; Liu et al., 2011).

$$\kappa = B \cdot \log(D_{\text{p}}(\text{Dry})) + C \cdot D_{\text{p}}(\text{Dry}) + D \quad (7)$$

Using this equation,  $\kappa_{\text{Mean}}$  was also parameterised. The fitting parameters are listed in Table 1; fitting results are presented in Fig. 5. No evident variations were found for  $\kappa_{\text{NH}}$ ,  $\kappa_{\text{LH}}$  and  $\kappa_{\text{MH}}$  with increasing dry

diameter. This indicated that inconsiderable change occurs in the types of chemical composition of each mode in aerosols with different diameters. With increasing particle size, however,  $N_{\text{FMH}}$  significantly increased from 0.30 to 70, while  $N_{\text{FLH}}$  and  $N_{\text{FNH}}$  decreased from 0.33 to 0.37 to 0.09 and 0.18. An increasing trend with size was accordingly exhibited by  $\kappa_{\text{Mean}}$ , with campaign averages of 0.16, 0.19, 0.21, 0.23 and 0.26 for 40, 80, 110, 150 and 200-nm aerosols, respectively. This revealed that the variation of  $\kappa_{\text{Mean}}$  was attributed to the change in the number fraction of each mode with increasing aerosol diameter. Furthermore, it was noteworthy that for 40-nm aerosols,  $N_{\text{FLH}}$  had the highest value, followed by  $N_{\text{FNH}}$ ; however,  $N_{\text{FMH}}$  was the highest for aerosols larger than 40 nm. This indicated that most of the 40-nm particles were dominated by the less hygroscopic and nearly hydrophobic particles, whereas aerosols larger than 40 nm were dominated by particles that were more hygroscopic.

Wu et al. (2016) and Wang et al. (2018d) also reported that in Beijing, the smaller particles had a higher fraction of NH or LH particles. A similar result was also found in Guangzhou (Jiang et al., 2016). This can be explained as follows. In the urban area, freshly emitted particles from traffic emissions and newly formed particles are major sources of particles smaller than 50 nm. Typically, freshly emitted particles (such as soot and water-insoluble organic matters) and newly formed particles (which are influenced by oxidation and condensation of VOCs) are initially nearly hydrophobic or less hygroscopic and externally mixed. In contrast, larger particles have undergone atmospheric ageing processes during transport for a longer time. The initially nearly hydrophobic or less hygroscopic aerosols can be rapidly coated by water-soluble inorganic aerosols, such as ammonium sulphate and ammonium nitrate, through coagulation, condensation and heterogeneous reactions of precursor gases, such as  $\text{SO}_2$  and  $\text{NO}_x$  (Pöschl, 2005). These ageing

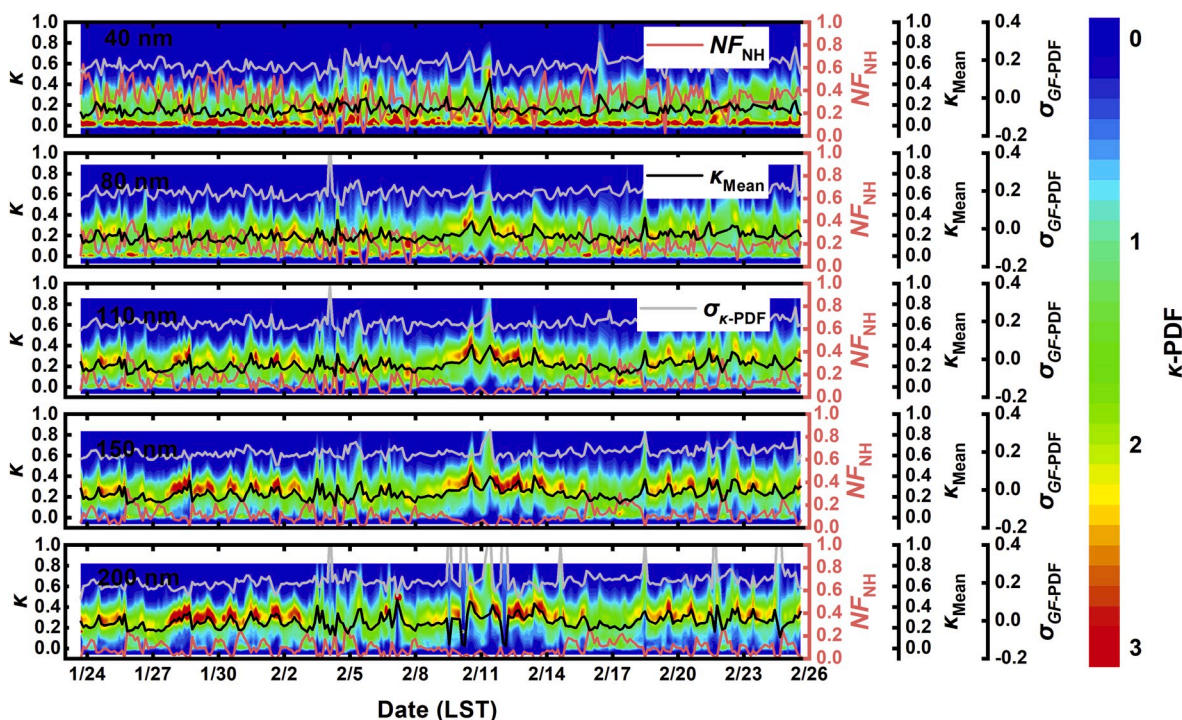


Fig. 4. Time series of  $\kappa$ -PDF, number fraction of nearly hydrophobic mode ( $NF_{NH}$ ), ensemble mean hygroscopicity parameter values ( $\kappa_{Mean}$ ) and standard deviation of GF-PDF ( $\sigma_{GF-PDF}$ ) for the five particle sizes measured during the Campaign.

processes enhance the hygroscopicity of aerosols (Jimenez et al., 2009; Liu et al., 2011).

To further facilitate the use of H-TDMA data, the parameterised  $GF$ s were calculated by solving Eq. (6) with  $\kappa$  values obtained from Eq. (7) using the parameters listed in Table 1. The ensemble mean  $GF$ s were therefore established as a function of  $RH$  and  $D_p$ (Dry); results are illustrated in Fig. 5. At a given  $RH$ ,  $GF$  increased with particle size, which was consistent with the measurements. The enhancement of  $GF$  was more significant at high  $RH$  levels, revealing the importance of the hygroscopic growth of aerosol particles under high  $RH$  conditions. This parameterisation could be employed to predict  $GF$  according to the ambient  $RH$  and dry particle sizes between 40 and 200 nm.

The typical characteristics of aerosol hygroscopicity at the megacities of the three majorly polluted areas in eastern China are summarised in Table 2. Similar to Beijing, Guangzhou and Shanghai, Chengdu is suffering from severe air pollution problems, particularly high  $PM_{2.5}$  loading during winter. It could be seen that  $\kappa_{Mean}$  for all measured sizes in Chengdu were lower than those in Shanghai (Ye et al., 2011, 2013) and Nanjing (Wu et al., 2014), which are two megacities located in the Yangtze River Delta. For the 150 and 200-nm aerosols, however,  $\kappa_{Mean}$  in Chengdu was slightly larger than those in Beijing and Guangzhou during winter. This might be the result of the accumulation of industrial and traffic emissions from the locality and around areas under the condition of high humidity and high static wind frequency in Chengdu (Liao et al.,

2018) that play an important function in the formation of hygroscopic salts, such as second inorganic aerosols (SNA, including  $SO_4^{2-}$ ,  $NO_3^-$  and  $NH_4^+$ ). The relatively higher hygroscopicity of aerosols larger than 110 nm indicated the stronger growth and more liquid water content of aerosols under the same  $RH$  conditions. The accumulation and hygroscopic growth of aerosols, thereafter, could contribute to more severe environmental effects than those in other cities.

### 3.2.3. Diurnal variation of aerosol hygroscopicity

Fig. 6 shows the average diurnal variations of  $NF_{NH}$ ,  $NF_{LH}$ ,  $NF_{MH}$  and  $\kappa_{Mean}$  for the five measured particle sizes;  $\kappa$ -PDF and  $\sigma_{GF-PDF}$  are also shown in Fig. 6. Generally,  $NF_{NH}$  exhibited low values, but  $\kappa_{Mean}$  showed high values during daytime. There were peaks in the variation of  $NF_{NH}$  in the morning and evening at the rush hours (from 06:00 to 09:00 and 18:00 to 20:00 LST) for all particle sizes measured. This phenomenon revealed more externally mixed aerosol were emitted by the traffics at this time. This also contributed to the peaks of  $\sigma_{GF-PDF}$ , which indicated the heterogeneity and complexity of particle composition. In the evening, thermal inversion formed at ground level and a number of externally mixed nearly hydrophobic particles (such as BC), which were emitted by local diesel trucks and heavy-duty vehicles, accumulated on the surface. This resulted in an increase in  $NF_{NH}$  and  $\sigma_{GF-PDF}$  but a decrease in  $\kappa_{Mean}$  at night. During daytime, more highly aged particles because of the photochemical reactions resulted in the decrease in  $NF_{NH}$  and increase in  $NF_{MH}$  and  $\kappa_{Mean}$ . With the corresponding decreasing  $\sigma_{GF-PDF}$  in the afternoon, it could be inferred that the externally mixed aerosols were changed to internally mixed ones. Similar results are observed in the North China Plain (Zhang et al., 2016; Wang et al., 2017).

For the 40-nm aerosols,  $\kappa_{Mean}$  increased with  $NF_{MH}$  in the early morning (07:00–09:00) and peaks at 09:00. This was because of the formation of nitrate, which is easily generated by the heterogeneous hydrolysis of  $N_2O_5$  on wet surfaces under the higher  $RH$  condition during this time (Huang et al., 2018). The amount of NO emitted by traffic during this time is considerably converted into  $NO_2$ , which reacts with OH to form gaseous  $HNO_3$  and subsequently transforms into  $NH_4NO_3$ .

Table 1

Fitting parameters for parameterisation of  $\kappa$  and number fraction ( $NF$ ) using Eq. (7) during entire campaign.

	B	C	D
$\kappa_{Mean}$	0.0862	0.00024	0.0105
$\kappa_{NH}$	-0.0238	0.00004	0.0582
$\kappa_{LH}$	-0.0546	0.00009	0.2121
$\kappa_{MH}$	-0.1561	0.00075	0.5471
$NF_{NH}$	-0.6554	0.00142	1.3185
$NF_{LH}$	0.0724	-0.00151	0.3175
$NF_{MH}$	0.6584	-0.00036	-0.7425

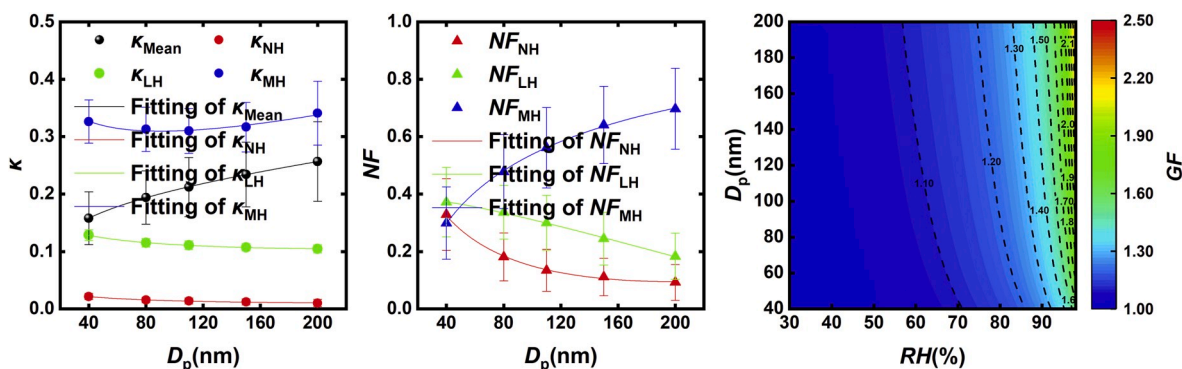


Fig. 5. Size-dependent (a)  $\kappa$  and (b)  $NF$  for NH, LH and MH modes ( $\kappa_{\text{NH}}$ ,  $\kappa_{\text{LH}}$ , and  $\kappa_{\text{MH}}$  and  $NF_{\text{NH}}$ ,  $NF_{\text{LH}}$ , and  $NF_{\text{MH}}$ , respectively) for the entire campaign and (c) the calculated  $GF$ s as functions of  $RH$  and  $D_p$ (Dry).

The decrease in  $\kappa_{\text{Mean}}$  from 09:00 to 11:00 could be explained by the collision and coagulation of 40-nm aerosols with larger ones. This was also the reason why  $NF_{\text{MH}}$  and  $\kappa_{\text{Mean}}$  for the other diameters peaked at 11:00–12:00. After 12:00, the enhanced solar radiation, high temperatures and low  $RH$  contributed to the decomposition of nitrate (e.g.,  $\text{NH}_4\text{NO}_3$ ), but were favourable to the formation of sulphuric and secondary organic aerosols (SOAs) during photochemical reactions. These SOAs, which are initially nearly hydrophobic or less hygroscopic, were concentrated in smaller sizes and their hygroscopicity could be enhanced with their oxidation degrees, leading to the peaks of  $NF_{\text{NH}}$  and  $NF_{\text{LH}}$  for the 40-nm aerosols at noon and then in the afternoon. This phenomenon affected the 40-nm diameter aerosols more evidently. With increasing diameter, however, the effects became less.

For aerosols with  $D_p > 80$  nm,  $NF_{\text{MH}}$  significantly increased during daytime. On the one hand, the condensable vapours, like sulphuric acid, could condense onto pre-existing particles, and SOAs formed by the strong photochemical reactions during daytime, could coagulate to larger particles and then enhance the water-absorbing capacity of these particles (Wu et al., 2016). On the other hand, the development of PBL after sunrise drew moderately aged and internally mixed aerosols from the upper layers to the surface. Furthermore, the particles that have been for a longer time in the atmosphere were more aged and consequently increased their hygroscopicity (Zhang et al., 2016; Jiang et al., 2016). This conclusion is supported by the diurnal cycles of the PNSDs and the secondary inorganic nitrate observed during the campaign. The previous study of water-soluble ions by Huang et al. (2018) in Chengdu also confirmed these diurnal patterns.

### 3.3. Case study

To further explore the variation in the hygroscopicity of submicron aerosols and the factors that influence this hygroscopicity, the case studies of three PEs and two clean periods (CPs) during the campaign are selected (Fig. 3). The PE is defined as the period during which the hourly  $\text{PM}_{2.5}$  exceeds  $75 \mu\text{g m}^{-3}$  during hours; similarly, the period with  $\text{PM}_{2.5}$  less than  $75 \mu\text{g m}^{-3}$  is recognised as CP.

Among the selected periods, PE1 (2019.1.23 00:00–2019.1.27 09:00), CP1 (2019.1.27 10:00–2019.1.28 20:00) and PE2 (2019.1.28 21:00–2019.1.30 15:00) are continuous periods before the Spring Festival (Fig. S2 and Fig. S3, the supplemental file); CP2 and PE3 (Fig. S4 and Fig. S5, the supplemental file) are periods after the Spring Festival. These selected periods make possible the comparison of differences in aerosol hygroscopicities before and after the Spring Festival.

Fig. 7 depicts the time series of  $\kappa$ -PDF,  $NF_{\text{NH}}$ ,  $\kappa_{\text{Mean}}$  and  $\sigma_{GF}$ -PDF during PE1, CP1 and PE2. The general variation of aerosol hygroscopicity has been previously analysed in Section 3.2.2. The average  $\kappa_{\text{Mean}}$  for aerosols with diameters of 40 and 80 nm during PE1 (0.14 and 0.18, respectively) were nearly the same as those in CP1 (0.15 and 0.18, respectively) but slightly larger than those in PE2 (0.12 and 0.17, respectively). For aerosols larger than 80 nm,  $\kappa_{\text{Mean}}$  values during PE1 and PE2 were lower than that in CP1. These changes were attributed to the variation in the number fraction of the three modes because  $\kappa$  for these modes were practically constant during all three periods (Table S1, the supplemental file).

For 40-nm aerosols,  $NF_{\text{NH}}$  in PE1 (0.39) was lower than that in PE2 (0.46) and both were higher than that in CP1 (0.32);  $NF_{\text{LH}}$  in PE1 and PE2 (0.33 and 0.31, respectively) were lower than that in CP1 (0.41).

Table 2  
Ensemble mean hygroscopicity parameter values ( $\kappa_{\text{Mean}}$ ) in different cities of China.

Site	Time	30 nm	40 nm	50 nm	80 nm	110 nm	150 nm	200 nm	250 nm
Nanjing, suburban (Wu et al., 2014)	2012 05–07		0.26		0.24	0.25	0.27	0.28	
Beijing, urban (Wu et al., 2016)	2014 summer			0.16		0.19 (100 nm)	0.22	0.26	0.28
Beijing, urban (Wang et al., 2018d)	2015 winter			0.12	0.19 (75 nm)	0.18 (100 nm)	0.18		0.16
Beijing, urban (Wang et al., 2018c)	2016 12			0.22		0.22 (100 nm)	0.22	0.22	
Beijing, urban (Massling et al., 2009)	2004 summer	0.10		0.14	0.17		0.21		0.24
	2005 winter	0.09		0.17	0.22		0.20		0.17
Guangzhou, urban (Tan et al., 2013b)	2011 winter		0.22		0.21	0.21	0.22	0.23	
Guangzhou, urban (Jiang et al., 2016)	2012 winter		0.18		0.19	0.20	0.21	0.22	
	2013 summer		0.17		0.18	0.18	0.20	0.21	
Shanghai, urban (Ye et al., 2011)	2009 02			0.24		0.28 (100 nm)		0.31	
Shanghai, urban (Ye et al., 2013)	2009 09	0.20		0.25	0.28	0.28 (100 nm)	0.29	0.31	
Chengdu, urban (This study)	2019 01–02		0.16		0.19	0.21	0.23	0.26	

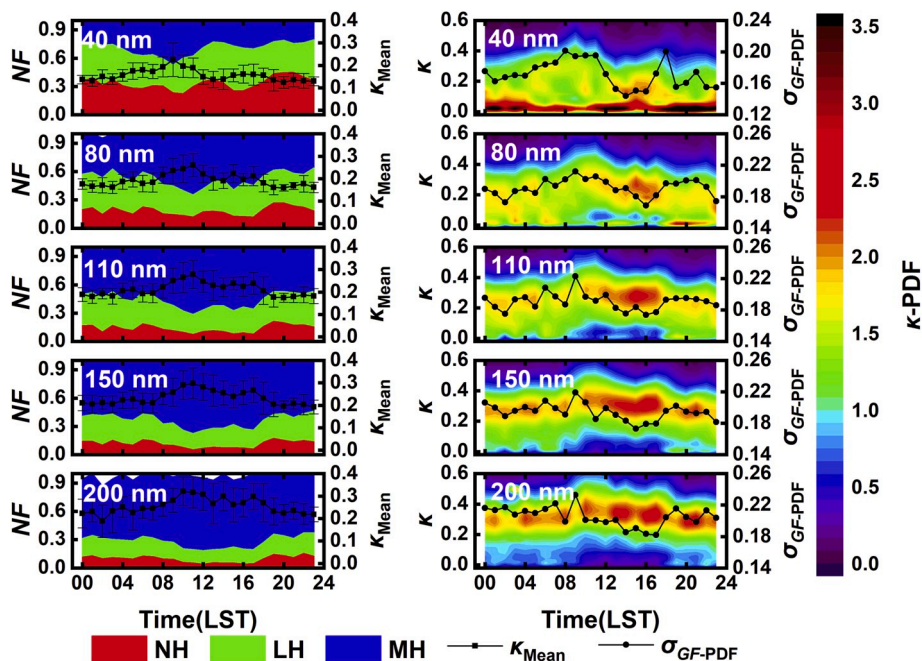


Fig. 6. Diurnal variations of the number fraction of each mode,  $\kappa_{Mean}$ ,  $\kappa$ -PDF and  $\sigma_{GF-PDF}$  for the five particle sizes measured during the Campaign.

The relatively larger  $NF_{NH}$  during PEs also revealed that there were more freshly emitted aerosols externally mixed during these periods. During CP1 (also in CP2),  $NF_{LH}$  was the largest and  $NF_{MH}$  has no increase compared to PE1 and PE2 (Table S1, the supplemental file), this was because the increasing number of SOAs formed by the secondary

transformation of precursors. Their degree of oxidation became higher during the atmospheric ageing progress on sunny days. Moreover, in the ageing progress, aerosols in the NH mode emitted during PE1 would gradually shift to the LH mode. This could be attributed to the second formation of inorganic salt on the surface of existing aerosols that are

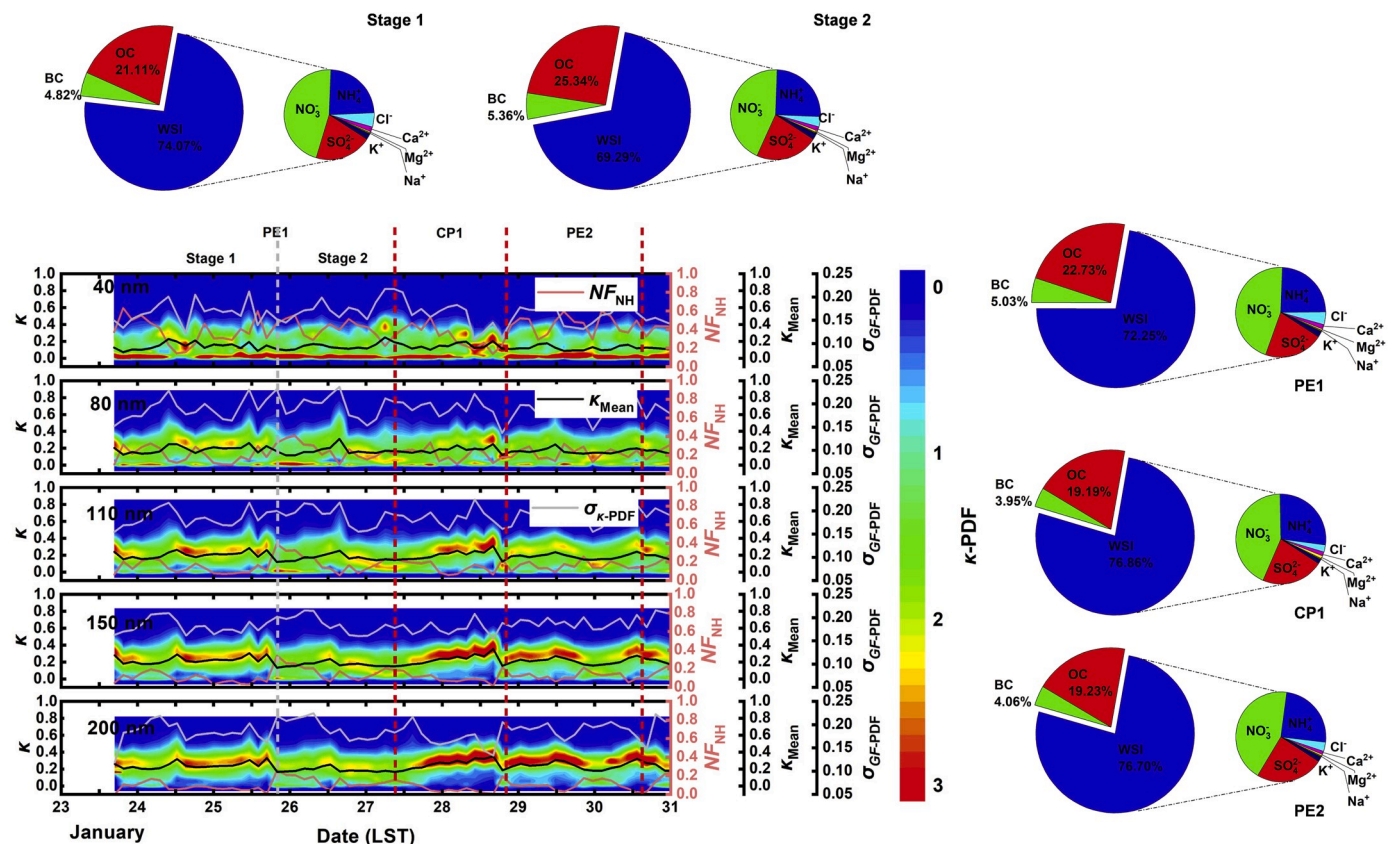


Fig. 7. Time series of  $\kappa$ -PDF,  $NF_{NH}$ ,  $\kappa_{Mean}$ ,  $\sigma_{GF-PDF}$  and percentage contribution of the major chemical components during pollution episode (PE) 1, clean period (CP) 1 and PE2.

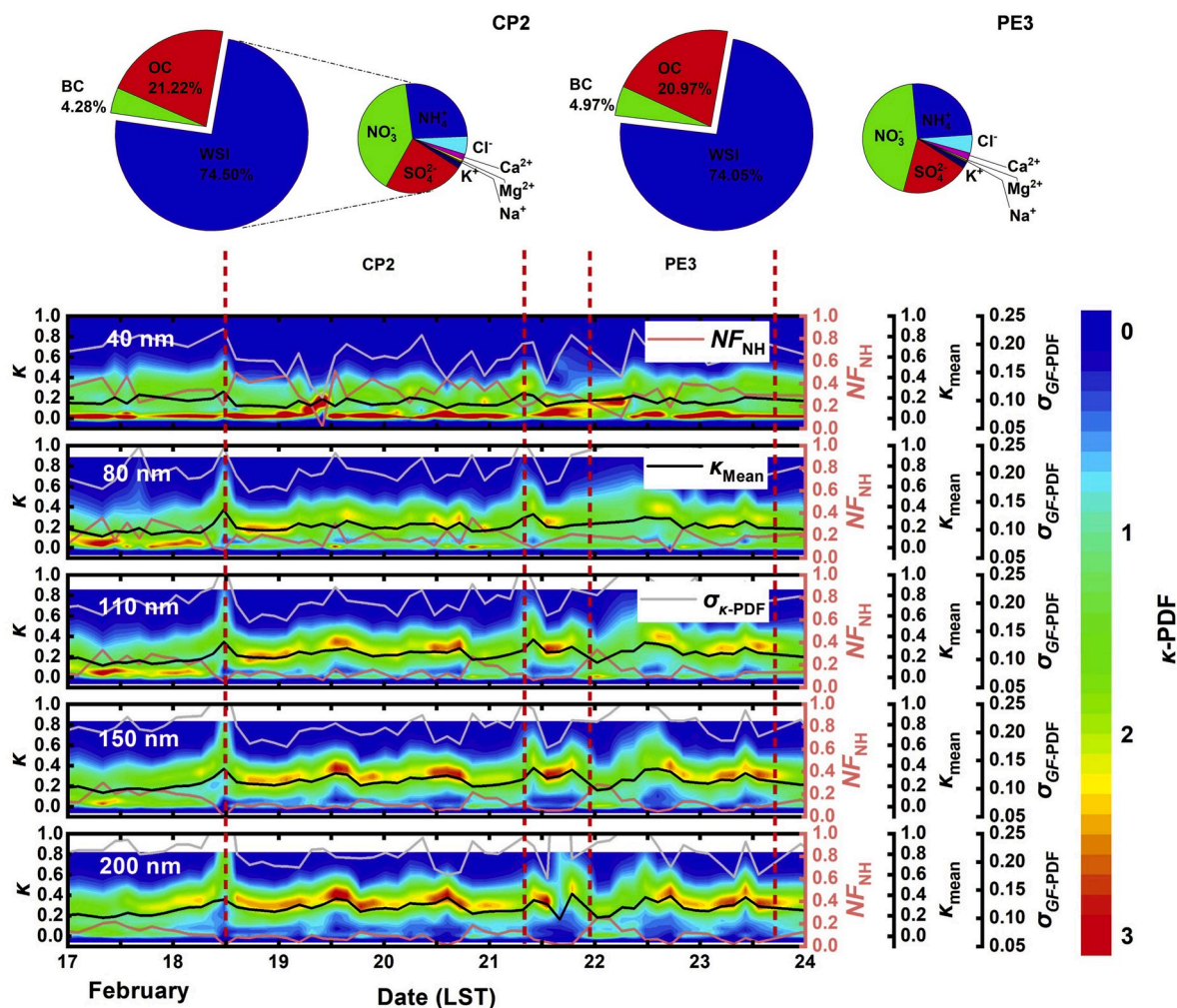


Fig. 8. Time series of  $\kappa$ -PDF,  $NF_{NH}$ ,  $\kappa_{Mean}$ ,  $\sigma_{GF-PDF}$  and percentage contribution of the major chemical components during CP2 and PE3.

larger than 40 nm. This led to the enhancement of the hygroscopicity of larger aerosols, as proved by the increase in  $NF_{MH}$  and  $\kappa_{Mean}$  in CP1 for aerosols larger than 80 nm.

For larger aerosols ( $D_p > 80$  nm),  $\kappa$ -PDF showed that PE1 experienced two distinct stages. It was easy to find that  $NF_{NH}$  was lower and  $\kappa_{Mean}$  was higher before 17:00 on 25 January; thereafter, the situation was exactly the opposite. Both  $NF_{NH}$  and  $NF_{LH}$  significantly increased and thus  $NF_{MH}$  became lower at Stage 2 (Table S2, the supplemental file). As shown in Fig. 7, evident increase of  $NF_{NH}$  and  $\sigma_{GF-PDF}$  could be found during the transition period from Stage 1 to Stage 2, indicating the enhancement of externally mixed aerosols because of primary emissions. Furthermore,  $\kappa$ -PDF became more concentrated with decreasing  $NF_{NH}$  during CP1 and PE2, during which distinctly different characteristics were exhibited compared with that during PE1. This revealed that the mixing state of aerosol particles changed during these two periods. More aerosols were internally mixed, especially in CP1, because of less emissions, thus contributing to the relatively higher  $\kappa_{Mean}$  than that in PE1. The similar trends of  $\kappa$ -PDF in CP1 and PE2 indicated the accumulative effect of local pollutants under the low wind condition. This was proved by the previous studies of Liao et al. (2017) and Wang et al., 2018 who demonstrated that the accumulation of local emissions was the main contributor to the pollution episodes in Chengdu.

Fig. 8 presents the time series of  $\kappa$ -PDF,  $NF_{NH}$ ,  $\kappa_{Mean}$  and  $\sigma_{GF-PDF}$  in CP2 and PE3. The characteristics of the size-resolved aerosol hygroscopicity did not differ with those in PE1, CP1 and PE2. During these two periods, however,  $\kappa_{Mean}$  values of all measured sizes were higher than

those in PE1, CP1 and PE2. Furthermore,  $\kappa_{Mean}$  in CP2 was lower than that in PE3 for all of the five sizes. It could be found that  $\kappa_{MH}$  during PE3 was higher than that in CP2 (Table S1, the supplemental file), indicating the presence of chemical species with a stronger hygroscopicity. This leads to a little bit higher  $\kappa_{Mean}$  in PE3 compared to that in CP2.

The statistical analysis indicated that the mass concentrations of  $PM_{2.5}$  in the PEs were 1.8–2.2 times higher than those in the CPs. The major chemical components, such as water-soluble inorganic ion (WSI), OC and BC, were 1.4–2.0, 1.5–2.0 and 1.5–2.3 times higher in the PEs than those in the CPs, respectively. In Figs. 7 and 8, the percentage contribution of the major chemical components to the detected chemical composition showed that the WSI was slightly lower and OC and BC were slightly higher in PE1. Generally, however, there were no significant differences during the selected periods. This result differed from those obtained in eastern China and North China Plain, where remarkable increases and decreases of fraction contribution were found for SNA and OC, respectively, in PEs compared to CPs (Wang et al., 2015). The practically similar trends of fractions in chemical compositions during PEs and CPs reaffirmed the accumulative effect of local pollutants. The different behaviours of hygroscopic properties between PEs and CPs and among different PEs, suggested that different and complicated processes existed in each episode.

Although aerosols with sizes measured during this campaign insignificantly contributed to the  $PM_{2.5}$  concentration, indicators could be found from the chemical composition of  $PM_{2.5}$  to determine the reasons that lead to the discrepancies between PEs and CPs. The relatively lower

fraction of WSI and the higher fractions of OC and BC resulted in the lower  $\kappa_{\text{Mean}}$  average in PE1 than in CP1 for larger aerosols. A thorough examination of the two distinct stages, which was divided by the distinct change of  $\kappa$  in PE1, showed that the percentage contribution of WSI to the detected chemical composition decreases from 74.1% in Stage 1–69.3% in Stage 2. The percentage contributions of OC and BC accordingly increased from 21.1% to 4.8% in Stage 1–25.3% and 5.4% in Stage 2, respectively. The varied fractions led to different hygroscopic properties in the two stages, particularly for aerosols larger than 80 nm. This was because the larger aerosol particles contributed more to the mass concentration of each component. According to the meteorological conditions and gaseous contaminants during Stages 1 and 2 (Figs. S2 and S3, respectively, the supplemental file), it could be seen that the average  $T$  in Stage 1 was the same as that in Stage 2 (8.8 °C), but the diurnal variation was relatively more distinct in Stage 1. The average  $RH$ , however, was relatively lower (70.0%) with a more evident diurnal cycle in Stage 1. These conditions were favourable to the formation of secondary aerosols (higher  $NF_{\text{LH}}$  and  $NH_{\text{MH}}$  for 40-nm aerosols). These aerosols then coagulated with larger ones, possibly enhancing the latter's hygroscopicity. The distinct diurnal patterns of  $\text{NO}_2$  and  $\text{O}_3$  also confirmed the intense photochemical reactions during Stage 1 wherein considerable amounts of hygroscopic substances were produced. This led to the higher  $\kappa_{\text{Mean}}$  in Stage 1 compared to that in Stage 2. Moreover, it was noteworthy that at the beginning of Stage 2, fresh emissions existed based on the variation of CO, BC and PNSDs. These aerosols were generally hydrophobic, resulting in the top values of  $\kappa$ -PDF in the NH mode, and thus, increase in  $NF_{\text{NH}}$  and  $\sigma_{\text{GF-PDF}}$  for all sizes measured and decrease in  $\kappa_{\text{Mean}}$  for aerosols larger than 40 nm. The rapid changes in the  $\kappa$ -PDF, the top in the NH mode disappeared and reappeared gradually in the LH and MH mode (also reflected by  $\sigma_{\text{GF-PDF}}$  variation), revealed that freshly emitted aerosols were externally mixed with pre-existing aerosols once they were emitted; thereafter, they rapidly aged. The same phenomenon was also observed when there were fresh emissions in the evening of 28 January, in the early morning of 30 January and during PE3.

In the latter part of Stage 2, there were less freshly emitted aerosols (i.e., with low values of  $NF_{\text{NH}}$ ) and the wind speed increased, the

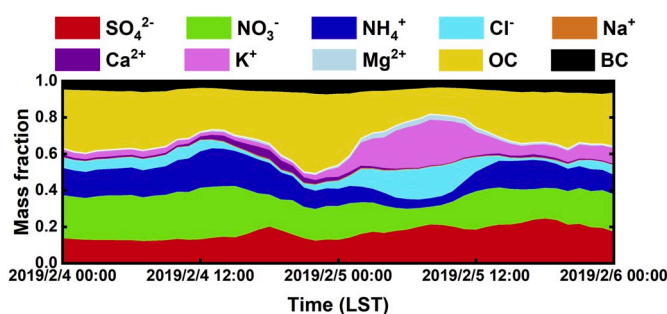


Fig. 10. Fraction contribution of the major chemical components during the FE.

pollutants started to dissipate. The pre-existing aerosols therefore increasingly became more aged, leading to the continuous increase in  $\kappa_{\text{Mean}}$ , accompanied by more aerosols becoming internally mixed during CP1 compared with that during PE1.

Furthermore, the comparable fraction of major chemical components led to the discrepancy of aerosol hygroscopic properties between CP2 and PE3. In examining each species in the WSI, it was observed that although the mass fraction of SNA slightly decreased in PE3, the percentage contribution of  $\text{SO}_4^{2-}$  decreased from 23.9% to 19.9% but  $\text{NO}_3^-$  increased from 39.9% to 44.4%. The nitrate has a stronger hygroscopicity than sulphate (Petters and Kreidenweis, 2007) and contributed to the higher  $\kappa_{\text{MH}}$  in PE3. The higher  $\kappa_{\text{Mean}}$  therefore was influenced by both the varied fraction of NH, LH and MH modes and the changed types of chemical composition in each mode. Moreover, the relatively higher  $\kappa_{\text{Mean}}$  but lower fraction contribution of WSI in CP2 and PE3 compared to that of CP1 and PE2 could also result from the increase in the component with a stronger hygroscopicity, such as NaCl, according to the chemical composition analysis in  $\text{PM}_{2.5}$ .

#### 3.4. Impact of fireworks on aerosol hygroscopicity

An FE during the Chinese New Year's Eve to the next day was

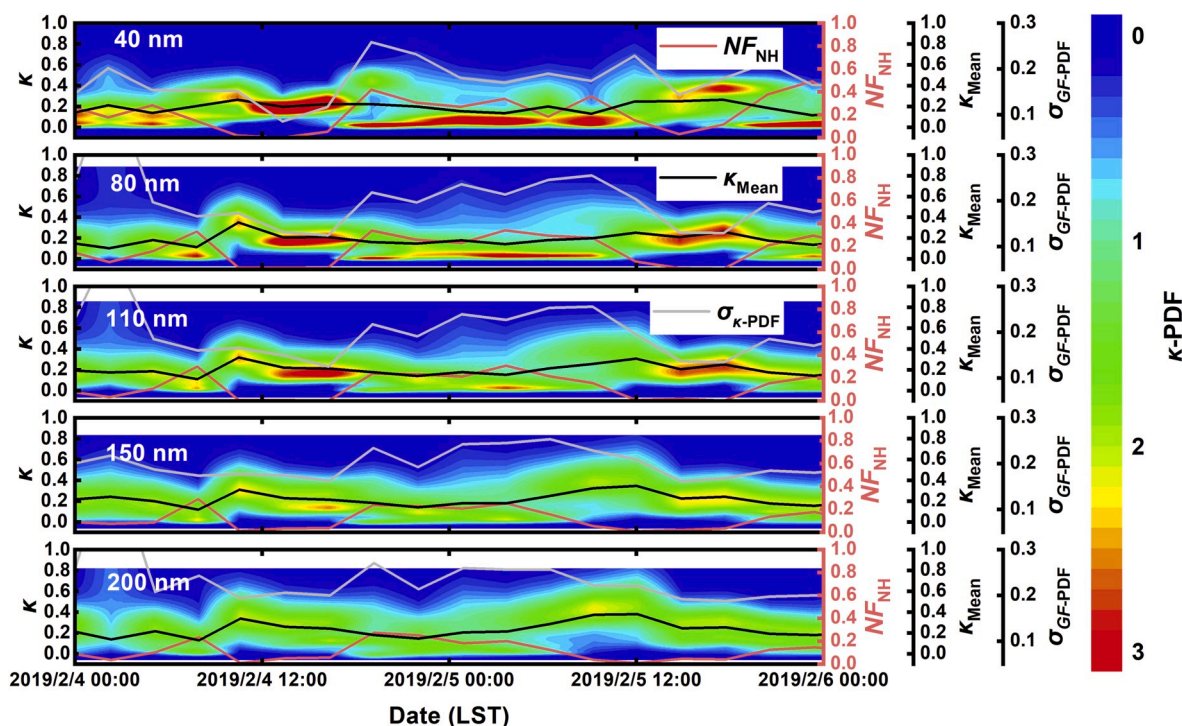


Fig. 9. Time series of  $\kappa$ -PDF,  $NF_{\text{NH}}$ ,  $\kappa_{\text{Mean}}$  and  $\sigma_{\text{GF-PDF}}$  during the fireworks episode (FE).

identified. It was characterised by the  $PM_{2.5}$  concentration that increased and remained above  $75 \mu\text{g}/\text{m}^3$ . The FE was thus recognised from 22:00 on 4 February to 16:00 on 5 February 2019 (Fig. S6) when numerous fireworks were lit to celebrate the Spring festival. The period was an opportune time to investigate the influence of fireworks on the hygroscopicity of submicron aerosols.

Prior to the FE,  $PM_{2.5}$  was low with a minimum of  $31.5 \mu\text{g}/\text{m}^3$  because of the vertical diffusion in the well-developed boundary layer on 4 February. In other cities, rapid increases in the mass concentration and amount of aerosol occurred at approximately midnight (00:00) (Wehner et al., 2000; Zhang et al., 2010; Kong et al., 2015; Tanda et al., 2019). The case in Chengdu differed in that slow and continuous growths of  $PM_{2.5}$ , BC, CO and  $SO_2$  mass concentrations that started in the afternoon of 4 February and increased to maximum values. These maximum values exceed  $470 \mu\text{g}/\text{m}^3$ ,  $17.7 \mu\text{g}/\text{m}^3$ ,  $1.1 \text{mg}/\text{m}^3$  and  $25.0 \mu\text{g}/\text{m}^3$ , respectively, at approximately 10:00 on 5 February and subsequently decreased until noon. The foregoing was simultaneously observed in several air quality stations in Chengdu, and similar elevated trends were also observed in the WSIs, such as  $SO_4^{2-}$ ,  $Na^+$ ,  $K^+$  and  $Cl^-$ . This indicated that Chengdu is still affected by the fireworks although the use of fireworks is forbidden. The fireworks from the surrounding areas that accumulate under low temperature, low wind, low PBL and high RH conditions during the night (Fig. S6, the supplemental file) was considered to have non-negligible influences, namely the “indirect” influences, on Chengdu. The variation in the PNSD showed that the aerosol number concentration was also low at noon on 4 February. A sudden peak in aerosol number concentration with diameter from 20 to more than 100 nm occurred in the afternoon and continued to the next day. This was consistent with aerosols that are typically generated by fireworks. They have a maximum number concentration with sizes widely range from lower than 50 nm to larger than 100 nm (Wehner et al., 2000; Zhang et al., 2010; Jing et al., 2014; Lin, 2016). The median diameter of aerosols also has a continuously increasing trend with the development of the FE (Fig. S7, the supplemental file), reconfirming the “indirect” influence and atmospheric ageing process.

For the hygroscopic properties, slow enhancements of  $\kappa_{\text{Mean}}$  could be found for aerosol diameters of 80, 110, 150 and 200 nm during the FE (Fig. 9). This pattern was consistent with the trends of  $Cl^-$ ,  $K^+$  and  $Na^+$  in  $PM_{2.5}$  (Fig. 10). Previous studies related to the major chemical components of fireworks generated aerosols also confirmed the elevation of  $Cl^-$ ,  $K^+$  and  $Na^+$  (Lin et al., 2014; Kong et al., 2015; Lin, 2016; Carrico et al., 2018). Note that KCl and NaCl are strongly hygroscopic salts (Carrico et al., 2010), led to average  $\kappa_{\text{MH}}$  values of 0.36, 0.35, 0.35 and 0.37 for 80, 110, 150 and 200-nm diameter aerosols, respectively, during the FE. These values were significantly higher than those on the pre-FE and post-FE days.

The average values of  $\kappa_{\text{NH}}$ ,  $\kappa_{\text{LH}}$  and  $\kappa_{\text{MH}}$  among the different sizes measured during the FE period did not considerably differ (Table S2, the supplemental file), indicating that the effects of fireworks were uniform on atmospheric submicron aerosols. The  $NF_{\text{MH}}$  values, however, were observed to have an increasing trend with size (from 0.34 for 40-nm aerosols to 0.64 for 200-nm aerosols), indicating that more strong hygroscopic components of fireworks were found in the larger aerosols. This resulted in increasing  $\kappa_{\text{Mean}}$  with increasing diameter; the  $\kappa_{\text{Mean}}$  averages were 0.19, 0.19, 0.21, 0.23 and 0.27 for the 40, 80, 110, 150 and 200-nm aerosols, respectively. These results, with values higher than those during the pre-FE and post-FE periods, indicated the severe threat to the environment.

The analyses that focus on fireworks aerosols demonstrate that the WSIs are critical parts of PM chemical compositions, and the fraction contribution of SNA gradually increases and becomes the major components of WSI during the post-FE periods (Yang et al., 2014; Kong et al., 2015). All of these components have a critical influence on the hygroscopicity of aerosols (Lin, 2016). In this study, a similar phenomenon was observed that the contributions of  $Cl^-$  and  $K^+$  were replaced by the SNA after the FE. Correspondingly,  $\kappa_{\text{Mean}}$  for all measured sizes

decreased with decreasing  $Cl^-$  and  $K^+$  fractions; the distribution of  $\kappa$ -PDF for the selected sizes became more concentrated with decreasing  $\sigma_{\text{GF-PDF}}$  (Note that the  $Na^+$  concentration was found to be approximately two orders of magnitude smaller than those of  $Cl^-$  and  $K^+$ . As a result, the change in its fraction contribution was not evident before, during and after the FE). This indicated the ageing of aerosols during the production of SNA in the post-FE atmosphere. The externally mixed fireworks aerosols therefore became gradually internal mixture.

Numerous studies alerted regarding the environmental and health risks of fireworks during big celebrations and festivals. The enhanced hygroscopicity of submicron aerosols during the FE reveals that more ultrafine aerosols, which are originally insensitive to light scattering, can grow into a size that can scatter more visible light at high RH. This contributes to the strong attenuation of incident solar radiation and visibility that is most easily noticed by the public in terms of aerosol environmental effect. The strong hygroscopicity also reveals the higher liquid water content of aerosols that can promote the chemical conversion of secondary aerosols on their surface; this can further cause serious health damage to humans. These effects can be amplified by the feedback cycle of higher hygroscopicity, stronger scattering and more water content, lower visibility and stronger chemical conversion and higher hygroscopicity. Moreover, the high hygroscopicity of fireworks increases the probability of cloud condensation nuclei activation to cloud droplets. This can lead to a higher activation ratio at a lower super-saturation, consequently increasing the number and decreasing the size of cloud droplets. It can also affect cloud optical properties, cloud cover and cloud lifetime. Further observations should therefore be implemented to more precisely quantify these effects and their interactions so that the results can be readily applied to the prediction of environmental and health effects as well as to the climate modelling.

#### 4. Conclusions

In-situ measurement of the size-resolved hygroscopic behaviour of submicron aerosols was conducted from late January to February, 2019, in a megacity in Sichuan Basin. The growth factors (GF) at 90% relative humidity for dry aerosol with diameters of 40, 80, 110, 150 and 200 nm were measured by a hygroscopicity tandem differential mobility analyser (H-TDMA). The impacts of pollution episodes and fireworks on the hygroscopicity of submicron aerosols were investigated.

Aerosol particles were usually externally mixed and consisted of nearly hydrophobic mode (NH), less hygroscopic mode (LH) and more hygroscopic mode (MH) in the urban area. The ensemble mean hygroscopicity parameter values ( $\kappa_{\text{Mean}}$ ) showed an increasing trend with size due to the coating of water-soluble inorganic aerosols in the atmospheric ageing processes. The campaign average of  $\kappa_{\text{Mean}}$  were 0.16, 0.19, 0.21, 0.23 and 0.26 for aerosols with diameters of 40, 80, 110, 150 and 200 nm, respectively.

The diurnal patterns of aerosol hygroscopicity and mixing state were influenced by the photochemical reactions and development of planetary boundary layer (PBL). The number fractions of NH ( $NF_{\text{NH}}$ ) was low, but  $\kappa_{\text{Mean}}$  was high during daytime because the photochemical reactions and the PBL activities produced more highly aged particles; correspondingly increased the fraction of internally mixed aerosols.

The different behaviours of hygroscopicity during pollution episodes (PEs) and clean periods (CPs) were mainly caused by the change in the number fraction of each mode. The  $NF_{\text{LH}}$  values of the 40-nm diameter aerosols in CPs were larger due to the increase in the amount of SOAs formed by the secondary transformation and higher degree of oxidation during the atmospheric ageing progress. More aerosols of diameters larger than 80 nm were internally mixed during CP1 and stage of pollution accumulation, resulting in the higher  $\kappa_{\text{Mean}}$  values. The presence of stronger hygroscopic components in the MH mode could contribute to the higher  $\kappa_{\text{Mean}}$ .

The hygroscopicity of the fireworks aerosols showed that more strong hygroscopic components of fireworks were found in the larger

aerosols. The average  $\kappa_{\text{Mean}}$  values were 0.19, 0.19, 0.21, 0.23 and 0.27 for the 40, 80, 110, 150 and 200-nm aerosols, respectively, during the FE. These values were higher than those in the pre-FE and post-FE days, indicating the potential environmental threat of these pollutants. The production of SNA in the post-FE atmosphere made the externally mixed fireworks aerosols become gradually internal mixture.

The  $\kappa_{\text{Mean}}$  obtained in this study were lower than those in Shanghai and Nanjing.  $\kappa_{\text{Mean}}$  for aerosols larger than 110 nm, however, were higher than those in Beijing and Guangzhou during winter. This indicated the stronger growth and more liquid water content of aerosols under the same RH conditions. Considering about the condition of high humidity and high static wind frequency in the Sichuan Basin, the accumulation and hygroscopic growth of aerosols could contribute to more severe environmental effects than those in other regions. Thus, quantitative hygroscopic properties of aerosols in urban areas are essential for understanding the formation and evolution of severe haze events in the Sichuan Basin in southwest China. Studies addressing the direct measurement of the hygroscopicity of aerosols, however, are scarce in this region. The findings of this study contribute to the preliminary understanding of the hygroscopic behaviour of urban aerosol particles in the Sichuan Basin, but further observations should be implemented to more precisely quantify its impacts so that the results can be readily applied to the prediction of environmental and health effects as well as to the climate modelling.

#### Declaration of competing interest

The authors declare that they have no known competing financial interests or personal relationships that could have appeared to influence the work reported in this paper.

#### CRedit authorship contribution statement

**Liang Yuan:** Conceptualization, Methodology, Investigation, Writing - original draft, Writing - review & editing, Visualization. **Xiaoling Zhang:** Writing - review & editing, Supervision, Funding acquisition. **Miao Feng:** Investigation, Data curation. **Xuan Liu:** Investigation, Visualization. **Yuzhang Che:** Methodology, Software, Resources. **Hanbing Xu:** Software, Formal analysis, Data curation. **Klaus Schaefer:** Writing - review & editing. **Shigong Wang:** Funding acquisition, Writing - review & editing. **Yunjun Zhou:** Funding acquisition, Writing - review & editing.

#### Acknowledgements

This work was supported by the National Key Research and Development Program of China (2018YFC0214002 and 2016YFA0602004), the Joint Open Project of KLME & CIC-FEMD, NUIST (KLME 201908), the Project of Science and Technology Plan of Sichuan Province (2018SZDZX0023 and 2018JY0011) and the Scientific Research Foundation of Chengdu University of Information Technology (KYTZ201814). We would like to gratefully thank for the technical supports provided by Beijing SAAK-Mar Environmental Instrument Ltd.

#### Appendix A. Supplementary data

Supplementary data to this article can be found online at <https://doi.org/10.1016/j.atmosenv.2020.117393>.

#### References

Müller, A., Miyazaki, Y., Aggarwal, S., Kitamori, Y., Boreddy, S., Kawamura, K., 2017. Effects of chemical composition and mixing state on size-resolved hygroscopicity and cloud condensation nuclei activity of submicron aerosols at a suburban site in northern Japan in summer. *J. Geophys. Res. Atmos.* 122, 9301–9318. <https://doi.org/10.1002/2017JD027286>.

- Adam, M., Putaud, J., Martins dos Santos, S., Dell'Acqua, A., Gruening, C., 2012. Aerosol hygroscopicity at a regional background site (Ispra) in Northern Italy. *Atmos. Chem. Phys.* 12, 5703–5717. <https://doi.org/10.5194/acp-12-5703-2012>.
- Alonso-Blanco, E., Gómez-Moreno, F., Artíñano, B., 2019. Size-resolved hygroscopicity of ambient submicron particles in a suburban atmosphere. *Atmos. Environ.* 213, 349–358. <https://doi.org/10.1016/j.atmosenv.2019.05.065>.
- Bauer, J., Yu, X., Cary, R., Laulainen, N., Berkowitz, C., 2009. Characterization of the sunset semi-continuous carbon aerosol analyzer. *J. Air Waste Manag. Assoc.* 59, 826–833. <https://doi.org/10.3155/1047-3289.59.7.826>.
- Bian, Y., Zhao, C., Ma, N., Chen, J., Xu, W.Y., 2014. A study of aerosol liquid water content based on hygroscopicity measurements at high relative humidity in the North China Plain. *Atmos. Chem. Phys.* 14, 6417–6426. <https://doi.org/10.5194/acp-14-6417-2014>.
- Boreddy, S., Kawamura, K., Haque, M., 2015. Long-term (2001–2012) observation of the modeled hygroscopic growth factor of remote marine TSP aerosols over the western North Pacific: impact of long-range transport of pollutants and their mixing states. *Phys. Chem. Chem. Phys.* 17, 29344–29353. <https://doi.org/10.1039/c5cp05315c>.
- Brock, C., Wagner, N., Anderson, B., Attwood, A., Beyersdorf, A., Campuzano-Jost, P., Carlton, A., Day, D., Diskin, G., Gordon, T., Jimenez, J., Lack, D., Liao, J., Markovic, M., Middlebrook, A., Ng, N., Perring, A., Richardson, M., Schwarz, J., Washenfelder, R., Welti, A., Xu, L., Ziemba, L., Murphy, D., 2016. Aerosol optical properties in the southeastern United States in summer Part 1: hygroscopic growth. *Atmos. Chem. Phys.* 16, 4987–5007. <https://doi.org/10.5194/acp-16-4987-2016>.
- Carrico, C., Rood, M., Ogren, J., Neussus, C., Wiedensohler, A., Heintzenberg, J., 2000. Aerosol optical properties at Sagres, Portugal during ACE-2. *Tellus B* 52, 694–715. <https://doi.org/10.1034/j.1600-0889.2000.00049.x>.
- Carrico, C., Petters, M., Kreidenweis, S., Sullivan, A., McMeeking, G., Levin, E., Engling, G., Malm, W., Collett, J., 2010. Water uptake and chemical composition of fresh aerosols generated in open burning of biomass. *Atmos. Chem. Phys.* 10, 5165–5178. <https://doi.org/10.5194/acp-10-5165-2010>.
- Carrico, C., Gomez, S., Dubey, M., Aiken, A., 2018. Low hygroscopicity of ambient fresh carbonaceous aerosols from pyrotechnics smoke. *Atmos. Environ.* 178, 101–108. <https://doi.org/10.1016/j.atmosenv.2018.01.024>.
- Chen, L., Jeng, F., Chen, C., Hsiao, T., 2003. Hygroscopic behavior of atmospheric aerosol in Taipei. *Atmos. Environ.* 37, 2069–2075. [https://doi.org/10.1016/S1352-2310\(03\)00071-2](https://doi.org/10.1016/S1352-2310(03)00071-2).
- Chen, J., Zhao, C., Ma, N., Yan, P., 2014. Aerosol hygroscopicity parameter derived from the light scattering enhancement factor measurements in the North China Plain. *Atmos. Chem. Phys.* 14, 8105–8118. <https://doi.org/10.5194/acp-14-8105-2014>.
- Cocker, R., Whitlock, N., Flagan, R., Seinfeld, J., 2001. Hygroscopic properties of Pasadena California aerosol. *Aerosol Sci. Technol.* 35, 637–647. <https://doi.org/10.1080/02786820120653>.
- Enroth, J., Mikkilä, J., Németh, Z., Kulmala, M., Salma, I., 2018. Wintertime hygroscopicity and volatility of ambient urban aerosol particles. *Atmos. Chem. Phys.* 18, 4533–4548. <https://doi.org/10.5194/acp-18-4533-2018>.
- Gysel, M., McFiggans, G., Coe, H., 2009. Inversion of tandem differential mobility analyser (TDMA) measurements. *J. Aerosol Sci.* 40, 134–151. <https://doi.org/10.1016/j.jaerosci.2008.07.013>.
- Herrmann, H., Schaefer, T., Tilgner, A., Styler, S., Weller, C., Teich, M., Otto, T., 2015. Tropospheric aqueous-phase chemistry: kinetics, mechanisms, and its coupling to a changing gas phase. *Chem. Rev.* 115, 4259–4334. <https://doi.org/10.1021/cr500447k>.
- Huang, X., Zhang, J., Luo, B., Wang, L., Tang, G., Liu, Z., Song, H., Zhang, W., Yuan, L., Wang, Y., 2018. Water-soluble ions in PM<sub>2.5</sub> during spring haze and dust periods in Chengdu, China: variations, nitrate formation and potential source areas. *Environ. Pollut.* 243, 1740–1749. <https://doi.org/10.1016/j.envpol.2018.09.126>.
- Jiang, R., Tan, H., Tang, L., Cai, M., Yin, Y., Li, F., Liu, L., Xu, H., Chan, P., Deng, X., Wu, D., 2016. Comparison of aerosol hygroscopicity and mixing state between winter and summer seasons in Pearl River Delta region, China. *Atmos. Res.* 169, 160–170. <https://doi.org/10.1016/j.atmosres.2015.09.031>.
- Jimenez, J., Canagaratna, M., Donahue, N., Prevot, A., Zhang, Q., Kroll, J., DeCarlo, P., Allan, J., Coe, H., Ng, N., Aiken, A., Docherty, K., Ulbrich, I., Grieshop, A., Robinson, A.L., Duplissy, J., Smith, J.D., Wilson, K.R., Lanz, V.A., Hueglin, C., Sun, Y., Tian, J., Laaksonen, A., Raatikainen, T., Rautiainen, J., Vaattovaara, P., Ehn, M., Kulmala, M., Tomlinson, J., Collins, D., Cubison, M., Dunlea, E., Huffman, J., Onasch, T., Alfarra, M., Williams, P., Bower, K., Kondo, Y., Schneider, J., Drewnick, F., Borrmann, S., Weimer, S., Demerjian, K., Salcedo, D., Cottrell, L., Griffin, R., Takami, A., Miyoshi, T., Hatakeyama, S., Shimono, A., Sun, J., Zhang, Y., Dzepina, K., Kimmel, J., Sueper, D., Jayne, J., Herndon, S., Trimborn, A., Williams, L., Wood, E., Middlebrook, A., Kolb, C., Baltensperger, U., Worsnop, D., 2009. Evolution of organic aerosols in the atmosphere. *Science* 326, 1525–1529. <https://doi.org/10.1126/science.1180353>.
- Jing, H., Li, Y., Zhao, J., Li, B., Sun, J., Chen, R., Gao, Y., Chen, C., 2014. Wide-range particle characterization and elemental concentration in Beijing aerosol during the 2013 Spring Festival. *Environ. Pollut.* 192, 204–211. <https://doi.org/10.1016/j.envpol.2014.06.003>.
- Jing, A., Zhu, B., Wang, H., Yu, X., An, J., Kang, H., 2019. Source apportionment of black carbon in different seasons in the northern suburb of Nanjing, China. *Atmos. Environ.* 201, 190–200. <https://doi.org/10.1016/j.atmosenv.2018.12.060>.
- Kamilli, K., Poulain, L., Held, A., Nowak, A., Birmili, W., Wiedensohler, A., 2014. Hygroscopic properties of the Paris urban aerosol in relation to its chemical composition. *Atmos. Chem. Phys.* 14, 737–749. <https://doi.org/10.5194/acp-14-737-2014>.
- Khalizov, A., Zhang, R., Zhang, D., Xue, H., Pagels, J., McMurry, P., 2009. Formation of highly hygroscopic soot aerosols upon internal mixing with sulfuric acid vapor. *J. Geophys. Res. Atmos.* 114, D05208. <https://doi.org/10.1029/2008JD010595>.

- Kim, N., Park, M., Yum, S., Park, J., Song, I., Shin, H., Ahn, J., Kwak, K.-H., Kim, H., Bae, G.-N., Lee, G., 2017. Hygroscopic properties of urban aerosols and their cloud condensation nuclei activities measured in Seoul during the MAPS-Seoul campaign. *Atmos. Environ.* 153, 217–232. <https://doi.org/10.1016/j.atmosenv.2017.01.034>.
- Kong, S., Li, L., Li, X., Yin, Y., Chen, K., Liu, D., Yuan, L., Zhang, Y., Shan, Y., Ji, Y., 2015. The impacts of firework burning at the Chinese Spring Festival on air quality: insights of tracers, source evolution and aging processes. *Atmos. Chem. Phys.* 15, 2167–2184. <https://doi.org/10.5194/acp-15-2167-2015>.
- Kuang, Y., Zhao, C., Tao, J., Ma, N., 2015. Diurnal variations of aerosol optical properties in the North China Plain and their influences on the estimates of direct aerosol radiative effect. *Atmos. Chem. Phys.* 15, 5761–5772. <https://doi.org/10.5194/acp-15-5761-2015>.
- Kuang, Y., Zhao, C., Tao, J., Bian, Y., Ma, N., Zhao, G., 2017. A novel method for deriving the aerosol hygroscopicity parameter based only on measurements from a humidified nephelometer system. *Atmos. Chem. Phys.* 17, 6651–6662. <https://doi.org/10.5194/acp-17-6651-2017>.
- Levy, M., Zhang, R., Zheng, J., Tan, H., Wang, Y., Molina, L., Takahama, S., Russell, L., Li, G., 2014. Measurements of submicron aerosols at the California–Mexico border during the Cal–Mex 2010 field campaign. *Atmos. Environ.* 88, 308–319. <https://doi.org/10.1016/j.atmosenv.2013.08.062>.
- Li, Q., Yin, Y., Gu, X., Yuan, L., Kong, S., Jiang, Q., Chen, K., Li, L., 2015. An observational study of aerosol hygroscopic growth factor and cloud condensation nuclei in Nanjing in summer. *China Environ. Sci.* 35, 337–346.
- Li, K., Li, J., Liggio, J., Wang, W., Ge, M., Liu, Q., Guo, Y., Tong, S., Li, J., Peng, C., Jing, B., Wang, D., Fu, P., 2017. Enhanced light scattering of secondary organic aerosols by multiphase reactions. *Environ. Sci. Technol.* 51, 1285–1292. <https://doi.org/10.1021/acs.est.6b03229>, 2017.
- Liao, T., Wang, S., Ai, J., Gui, K., Duan, B., Zhao, Q., Zhang, X., Jiang, W., Sun, Y., 2017. Heavy pollution episodes, transport pathways and potential sources of PM<sub>2.5</sub> during the winter of 2013 in Chengdu (China). *Sci. Total Environ.* 584, 1056–1065. <https://doi.org/10.1016/j.scitotenv.2017.01.160>.
- Liao, T., Gui, K., Jiang, W., Wang, S., Wang, B., Zeng, Z., Che, H., Wang, Y., Sun, Y., 2018. Air stagnation and its impact on air quality during winter in Sichuan and Chongqing, southwestern China. *Sci. Total Environ.* 635, 576–585. <https://doi.org/10.1016/j.scitotenv.2018.04.122>.
- Lin, C., 2016. A review of the impact of fireworks on particulate matter in ambient air. *J. Air Waste Manag. Assoc.* 66, 1171–1182. <https://doi.org/10.1080/10962247.2016.1219280>.
- Lin, C., Huang, K., Chen, H., Tsai, J., Chiu, Y., Lee, J., Chen, S., 2014. Influences of beehive firework displays on ambient fine particles during the Lantern Festival in the YanShuei area of southern Taiwan. *Aerosol Air Qual. Res.* 14, 1998–2009. <https://doi.org/10.4209/aaqr.2014.09.0201>.
- Liu, B., Pui, D., Whitby, K., Kittelson, D., Kousaka, Y., McKenzie, R., 1978. The aerosol mobility chromatograph: a new detector for sulfuric acid aerosols. *Atmos. Environ.* 12, 99–104. [https://doi.org/10.1016/0004-6981\(78\)90192-0](https://doi.org/10.1016/0004-6981(78)90192-0).
- Liu, P., Zhao, C., Göbel, T., Hallbauer, E., Nowak, A., Ran, L., Xu, W., Deng, Z., Ma, N., Mildenerberger, K., Henning, S., Stratmann, F., Wiedensohler, A., 2011. Hygroscopic properties of aerosol particles at high relative humidity and their diurnal variations in the North China Plain. *Atmos. Chem. Phys.* 11, 3479–3494. <https://doi.org/10.5194/acp-11-3479-2011>.
- Liu, X., Gu, J., Li, Y., Cheng, Y., Qu, Y., Han, T., Wang, J., Tian, H., Chen, J., Zhang, Y., 2013a. Increase of aerosol scattering by hygroscopic growth: observation, modeling, and implications on visibility. *Atmos. Res.* 132–133, 91–101. <https://doi.org/10.1016/j.atmosres.2013.04.007>.
- Liu, X., Li, J., Qu, Y., Han, T., Hou, L., Gu, J., Chen, C., Yang, Y., Liu, X., Yang, T., Zhang, Y., Tian, H., Hu, M., 2013b. Formation and evolution mechanism of regional haze: a case study in the megacity Beijing, China. *Atmos. Chem. Phys.* 13, 4501–4514. <https://doi.org/10.5194/acp-13-4501-2013>.
- Liu, F., Tan, Q., Jiang, X., Yang, F., Jiang, W., 2019. Effects of relative humidity and PM<sub>2.5</sub> chemical compositions on visibility impairment in Chengdu, China. *J. Environ. Sci.* 86, 15–23. <https://doi.org/10.1016/j.jes.2019.05.004>.
- Massling, A., Stock, M., Wiedensohler, A., 2005. Diurnal, weekly, and seasonal variation of hygroscopic properties of sub-micrometer urban aerosol particles. *Atmos. Environ.* 39, 3911–3922. <https://doi.org/10.1016/j.atmosenv.2005.03.020>.
- Massling, A., Stock, M., Wehner, B., Wu, Z., Hu, M., Brüggemann, E., Gnauk, T., Herrmann, H., Wiedensohler, A., 2009. Size segregated water uptake of the urban submicrometer aerosol in Beijing. *Atmos. Environ.* 43, 1578–1589. <https://doi.org/10.1016/j.atmosenv.2008.06.003>.
- Ning, G., Wang, S., Yim, S., Li, J., Hu, Y., Shang, Z., Wang, J., Wang, J., 2018. Impact of low-pressure systems on winter heavy air pollution in the northwest Sichuan Basin, China. *Atmos. Chem. Phys.* 18, 13601–13615. <https://doi.org/10.5194/acp-18-13601-2018>.
- Petters, M., Kreidenweis, S., 2007. A single parameter representation of hygroscopic growth and cloud condensation nucleus activity. *Atmos. Chem. Phys.* 7, 1961–1971. <https://doi.org/10.5194/acp-7-1961-2007>.
- Pöschl, U., 2005. Atmospheric aerosols: composition, transformation, climate and health effects. *Angew. Chem.-Int. Ed.* 44, 7520–7541. <https://doi.org/10.1002/anie.200501122>.
- Rissler, J., Vestin, A., Swietlicki, E., Fisch, G., Zhou, J., Artaxo, P., Andreae, M., 2006. Size distribution and hygroscopic properties of aerosol particles from dry-season biomass burning in Amazonia. *Atmos. Chem. Phys.* 6, 471–491. <https://doi.org/10.5194/acp-6-471-2006>.
- Sjogren, S., Gysel, M., Weingartner, E., Alfarra, M., Duplissy, J., Cozic, J., Crosier, J., Coe, H., Baltensperger, U., 2008. Hygroscopicity of the submicrometer aerosol at the high-alpine site Jungfraujoch, 3580 m a.s.l., Switzerland. *Atmos. Chem. Phys.* 8, 5715–5729. <https://doi.org/10.5194/acp-8-5715-2008>.
- Štefančová, L., Schwarz, J., Maenhaut, W., Chi, X., Smolík, J., 2010. Hygroscopic growth of atmospheric aerosol sampled in Prague 2008 using humidity controlled inlets. *Atmos. Res.* 98, 237–248. <https://doi.org/10.1016/j.atmosres.2010.04.009>.
- Stolzenburg, M., McMurry, P., 2008. Equations governing single and tandem DMA configurations and a new lognormal approximation to the transfer function. *Aerosol Sci. Technol.* 42, 421–432. <https://doi.org/10.1080/02786820802157823>.
- Swietlicki, E., Hansson, H., HÄMeri, K., Svenningsson, B., Massling, A., McFiggans, G., McMurry, P., PetÄJA, T., Tunved, P., Gysel, M., Topping, D., Weingartner, E., Baltensperger, U., Rissler, J., Wiedensohler, A., Kulmala, M., 2008. Hygroscopic properties of submicrometer atmospheric aerosol particles measured with H-TDMA instruments in various environments—a review. *Tellus B* 60, 432–469. <https://doi.org/10.1111/j.1600-0889.2008.00350.x>.
- Tan, H., Xu, H., Wan, Q., Li, F., Deng, X., Chan, P., Xia, D., Yin, Y., 2013a. Design and application of an unattended multifunctional H-TDMA system. *J. Atmos. Ocean. Technol.* 30, 1136–1149. <https://doi.org/10.1175/JTECH-D-12-00129.1>.
- Tan, H., Yin, Y., Gu, X., Li, F., Chan, P., Xu, H., Deng, X., Wan, Q., 2013b. An observational study of the hygroscopic properties of aerosols over the Pearl River Delta region. *Atmos. Environ.* 77, 817–826. <https://doi.org/10.1016/j.atmosenv.2013.05.049>.
- Tan, F., Tong, S., Jing, B., Hou, S., Liu, Q., Li, K., Zhang, Y., Ge, M., 2016. Heterogeneous reactions of NO<sub>2</sub> with CaCO<sub>3</sub>(NH<sub>4</sub>)<sub>2</sub>SO<sub>4</sub> mixtures at different relative humidities. *Atmos. Chem. Phys.* 16, 8081–8093. <https://doi.org/10.5194/acp-16-8081-2016>.
- Tanda, S., Ličbinský, R., Hegrová, J., Goessler, W., 2019. Impact of New Year's Eve fireworks on the size resolved element distributions in airborne particles. *Environ. Int.* 128, 371–378. <https://doi.org/10.1016/j.envint.2019.04.071>.
- Tao, W., Chen, J., Li, Z., Wang, C., Zhang, C., 2012. Impact of aerosols on convective clouds and precipitation. *Rev. Geophys.* 50, 1–62. <https://doi.org/10.1029/2011RG000369>.
- Tao, J., Zhao, C., Ma, N., Liu, P., 2014. The impact of aerosol hygroscopic growth on the single-scattering albedo and its application on the NO<sub>2</sub> photolysis rate coefficient. *Atmos. Chem. Phys.* 14, 12055–12067. <https://doi.org/10.5194/acp-14-12055-2014>.
- Tie, X., Huang, R., Cao, J., Zhang, Q., Cheng, Y., Su, H., Chang, D., Pöschl, U., Hofmann, T., Dusek, U., Li, G., Worsnop, D., O'Dowd, C., 2017. Severe pollution in China amplified by atmospheric moisture. *Sci. Rep.* 7, 15760. <https://doi.org/10.1038/s41598-017-15909-1>.
- Wang, Y., Li, Z., Zhang, Y., Du, W., Zhang, F., Tan, H., Xu, H., Fan, T., Jin, X., Fan, X., Dong, X., Wang, Q., Sun, Y., 2018b. Characterization of aerosol hygroscopicity, mixing state, and CCN activity at a suburban site in the central North China Plain. *Atmos. Chem. Phys.* 18, 11739–11752. <https://doi.org/10.5194/acp-18-11739-2018>.
- Wang, H., Qiao, L., Lou, S., Zhou, M., Chen, J., Wang, Q., Tao, S., Chen, C., Huang, H., Li, L., Huang, C., 2015. PM<sub>2.5</sub> pollution episode and its contributors from 2011 to 2013 in urban Shanghai, China. *Atmos. Environ.* 123, 298–305. <https://doi.org/10.1016/j.atmosenv.2015.08.018>.
- Wang, Y., Zhang, F., Li, Z., Tan, H., Xu, H., Ren, J., Zhao, J., Du, W., Sun, Y., 2017. Enhanced hydrophobicity and volatility of submicron aerosols under severe emission control conditions in Beijing. *Atmos. Chem. Phys.* 17, 5239–5251. <https://doi.org/10.5194/acp-17-5239-2017>.
- Wang, X., Shen, X., Sun, J., Zhang, X., Wang, Y., Zhang, Y., Wang, P., Xia, C., Qia, X., Zhong, J., 2018a. Size-resolved hygroscopic behavior of atmospheric aerosols during heavy aerosol pollution episodes in Beijing in December 2016. *Atmos. Environ.* 194, 188–197. <https://doi.org/10.1016/j.atmosenv.2018.09.041>.
- Wang, H., Tian, M., Chen, Y., Shi, G., Liu, Y., Yang, F., Zhang, L., Deng, L., Yu, J., Peng, C., Cao, X., 2018d. Seasonal characteristics, formation mechanisms and source origins of PM<sub>2.5</sub> in two megacities in Sichuan Basin, China. *Atmos. Chem. Phys.* 18, 865–881. <https://doi.org/10.5194/acp-18-865-2018>.
- Wang, Y., Wu, Z., Ma, N., Wu, Y., Zeng, L., Zhao, C., Wiedensohler, A., 2018c. Statistical analysis and parameterization of the hygroscopic growth of the sub-micrometer urban background aerosol in Beijing. *Atmos. Environ.* 175, 184–191. <https://doi.org/10.1016/j.atmosenv.2017.12.003>.
- Wehner, B., Wiedensohler, A., Heintzenberg, J., 2000. Submicrometer aerosol size distributions and mass concentration of the Millennium fireworks 2000 in Leipzig, Germany. *J. Aerosol Sci.* 31, 1489–1493. [https://doi.org/10.1016/S0021-8502\(00\)00039-2](https://doi.org/10.1016/S0021-8502(00)00039-2).
- Wu, Y., Yin, Y., Gu, X., Tan, H., 2014. An observational study of the hygroscopic properties of aerosols in north suburb of Nanjing. *China Environ. Sci.* 34, 1938–1949.
- Wu, Z., Zheng, J., Shang, D., Du, Z., Wu, Y., Zeng, L., Wiedensohler, A., Hu, M., 2016. Particle hygroscopicity and its link to chemical composition in the urban atmosphere of Beijing, China, during summertime. *Atmos. Chem. Phys.* 16, 1123–1138. <https://doi.org/10.5194/acp-16-1123-2016>.
- Yang, L., Gao, X., Wang, X., Nie, W., Wang, J., Gao, R., Xu, P., Shou, Y., Zhang, Q., Wang, W., 2014. Impacts of firecracker burning on aerosol chemical characteristics and human health risk levels during the Chinese New Year Celebration in Jinan, China. *Sci. Total Environ.* 476–477, 57–64. <https://doi.org/10.1016/j.scitotenv.2013.12.110>.

- Ye, X., Ma, Z., Hu, D., Yang, X., Chen, J., 2011. Size-resolved hygroscopicity of submicrometer urban aerosols in Shanghai during wintertime. *Atmos. Res.* 99, 353–364. <https://doi.org/10.1016/j.atmosres.2010.11.008>.
- Ye, X., Tang, C., Yin, Z., Chen, J., Ma, Z., Kong, L., Yang, X., Gao, W., Geng, F., 2013. Hygroscopic growth of urban aerosol particles during the 2009 Mirage-Shanghai Campaign. *Atmos. Environ.* 64, 263–269. <https://doi.org/10.1016/j.atmosenv.2012.09.064>.
- Yeung, M., Lee, B., Li, Y., Chan, C., 2014. Simultaneous HTDMA and HR-ToF-AMS measurements at the HKUST supersite in Hong Kong in 2011. *J. Geophys. Res.* Atmos. 119, 9864–9883. <https://doi.org/10.1002/2013JD021146>.
- Zhang, M., Wang, X., Chen, J., Cheng, T., Wang, T., Yang, X., Gong, Y., Geng, F., Chen, C., 2010. Physical characterization of aerosol particles during the Chinese New Year's firework events. *Atmos. Environ.* 44, 5191–5198. <https://doi.org/10.1016/j.atmosenv.2010.08.048>.
- Zhang, S., Ma, N., Kecorius, S., Wang, P., Hu, M., Wang, Z., Größ, J., Wu, Z., Wiedensohler, A., 2016a. Mixing state of atmospheric particles over the North China Plain. *Atmos. Environ.* 125, 152–164. <https://doi.org/10.1016/j.atmosenv.2015.10.053>.
- Zieger, P., Fierz-Schmidhauser, R., Weingartner, E., Baltensperger, U., 2013. Effects of relative humidity on aerosol light scattering: results from different European sites. *Atmos. Chem. Phys.* 13, 10609–10631. <https://doi.org/10.5194/acp-13-10609-2013>.